Nonlinear Response of Nanoelectromechanical Resonators in Trapped Superfluid Vortex States

Nathaniel Morrison, B.S.
Department of Physics
Lancaster University

A thesis submitted for the degree of
Master of Science

July, 2021

Declaration

I declare that the work presented in this thesis is, to the best of my knowledge and belief, original and my own work. The material has not been submitted, either in whole or in part, for a degree at this, or any other university. This thesis does not exceed the maximum permitted word length of 35,000 words including appendices and footnotes, but excluding the bibliography. A rough estimate of the word count is: 14686

Nathaniel Morrison

Nonlinear Response of Nanoelectromechanical Resonators in Trapped Superfluid Vortex States

Nathaniel Morrison, B.S..
Department of Physics, Lancaster University
A thesis submitted for the degree of *Master of Science*. July, 2021

Abstract

Nanoelectromechanical resonators are useful as both probes and generators of turbulence in superfluid helium. Individual quantum vortices may become "trapped" by a doubly-clamped beam-type resonator, permitting probing of a single vortex line in isolation. This opens the door for studies of the fundamental processes governing the transfer and dissipation of energy in quantum turbulence at the smallest of length scales. As the small-scale limit of the Kelvin cascade is as yet poorly investigated, this is of great interest in the drive to understand how energy is ultimately returned to the environment in turbulent superfluid. In this thesis, evidence of single-vortex dynamics directly influencing resonator response is presented, via analysis of the transmission of a doubly-clamped beam resonator in the presence of quantum vortices. A length of vortex extending from the resonator beam to the substrate results in greatly increased dissipation, damping, and turbulence nucleation. The vortex also introduces a large, negative nonlinear restoring force. These effects are attributed to the motion of the vortex filament. These results demonstrate the ability of the nanoelectromechanical scheme to transduce motion on single vortex lines and recommends the system for future studies investigating the evolution of Kelvin waves.

Acknowledgements

I would like to thank first and foremost my advisor, Dr. Sergey Kafanov. Dr. Kafanov is an amazing physicist and superb teacher, and I learned even more than I expected to about not just superfluids but electronics, nanomechanics, and planning and carrying out physics experiments in general. I very much enjoyed our animated discussions as we tried to figure out why our little beams were wiggling in such weird ways. It goes without saying that this work would not have been possible without him.

I would like to thank Dr. Yuri Pashkin and Dr. George Pickett for their invaluable help in building the physical models of our system. They have an expansive knowledge of superfluid physics, and discussions with them were integral to matching our experimental observations with the physical behaviours of the NEMS.

As well as working with me on the theory, I would like to thank Dr. Viktor Tsepelin for his aid in developing the modelling software created for this study. I found great inspiration talking with Dr. Tsepelin and studying how he structured his programs.

I would like to thank Dr. Andrew Guthrie for laying the groundwork for this study. I may have made my own expansions, but it was fundamentally Dr. Guthrie's code that ran our instruments. During his doctorate program he pioneered the techniques we use to generate, trap, and probe our vortices, and his very well-written thesis was my primary resource as I learned what we were doing and why we were doing it when I first arrived.

I would like to thank Callum Hayward and Joe Depellette for working with me on the experimental system. Their company made learning how to work the network analyser much more pleasant.

I would like to thank Searbhán Patton for keeping me company during the long, cold, pandemic-choked winter in the lab. Though he was working on something completely different, he was always willing to let me bounce ideas off him.

Finally, I would like to thank the US-UK Fulbright Program for its generous financial support, without which this amazing adventure would not have been possible.

Contents

List of Figures

List of Tables

Chapter 1

Introduction

Turbulence in fluids is an exceedingly common and impactful phenomenon that is nevertheless little understood. The complex interplay of chaos, randomness, and, especially in real systems, external influences hinders attempts at finding rigorous, general descriptions of behaviours in turbulent fluids[4]. The famous Navier-Stokes equations well describe such systems, but the character and, in many cases, even the existence of their solutions remains an open problem[5].

A firm understanding of how energy is transferred into, through, and out of a turbulent fluid is, however, essential in solving a vast number of problems in both pure and applied science. Turbulence must be accounted for in the design of vehicles[6], buildings[7], and electric generators[8]. It is a major hurdle in the development of viable fusion power[9]. It is an essential process in the evolution of nebula and galaxies[10]. Current work on classical fluid dynamics centres primarily around statistical descriptions of turbulence, attempting to predict average behaviour on large space and time scales[11]. In many cases, however, a more fundamental understanding of the small scale nonlinear processes that give rise to these average behaviours would be very beneficial.

In recent years, quantum turbulence, particularly in superfluid, has emerged as a possible means of investigating these fundamental processes in a much less chaotic environment. Quantum turbulence is the manifestation of turbulent flow in non-classical fluids such as superfluids[1] and quantum gases[12]. Rather than the complex, hierarchical structure of vortices of ever-changing size seen in classical systems, quantum turbulence consists of tangles of vortex lines each possessing, in almost all cases, a single quantum of circulation[1]. Despite this dramatic departure from classical vorticity, the behaviour of these quantized vortices as they interact with each other and their environment, transfer and dissipate energy, and move through the fluid has shown promising parallels to classical turbulence[13–15]. A rigorous description of quantum turbulence may therefore be the key to a more rigorous description of

macroscopic turbulence.

In this paper, the interaction of quantized vortices in superfluid ^{4}He with a nanoelectromechanical resonator (NEMS) is described. The NEMS demonstrates highly nonlinear behaviour when a vortex becomes partially aligned with the oscillating beam. Experimental observations of this behaviour provide insight into the dissipation mechanisms governing the cascade of energy to smaller length scales in quantum turbulence, and indicate the potential utility of this measurement scheme in probing Kelvin waves along individual vortices. By modelling the NEMS-vortex system as a driven-damped Duffing oscillator, the degree of nonlinearity in the response of the resonator is quantified and its dependence upon resonator drive force is investigated.

1.1 Superfluids

A superfluid is a non-classical state of matter which behaves as a liquid possessing zero viscosity[1]. The superfluid state has been achieved using a number of elements and isotopes, including ^{3}He[16], ^{4}He[17], and a mixture of ^{6}Li and ^{7}Li[18]. The most commonly studied superfluid is ^{4}He, having a comparatively high lambda transition temperature T_λ - the point at which the fluid begins transitioning to the superfluid phase - of around 2.17 K.

1.1.1 Superfluid ^{4}He

The superfluidity of low-temperature ^{4}He is a product of Bose-Einstein condensation (BEC)[1]. Below the lambda transition temperature ^{4}He atoms begin to condense, occupying the same quantum ground state. Near the lambda point, however, most of the fluid remains in the classical state. This is the basis for the "two-fluid model", a common description of ^{4}He below 2.17 K[19]. The two-fluid model assumes that the normal fluid fraction and superfluid fraction behave as two mixed, non-interacting fluids, with the normal fluid fraction declining asymptotically to zero as temperature approaches 0 K. A qualitative plot of the normal and superfluid fractions as a function of temperature can be seen in Fig. 1.1. The mixture of normal and superfluid phases is known simply as "He-II". The lack of viscosity in the superfluid component allows for dissipationless flow in He-II so long as the velocity of the fluid does not exceed a critical velocity v_c.

1.1.2 Critical velocity in superfluid

Both superfluids and other BECs exhibit a critical velocity above which superflow breaks down. In a superconductor, often viewed as a superfluid of Cooper pairs,

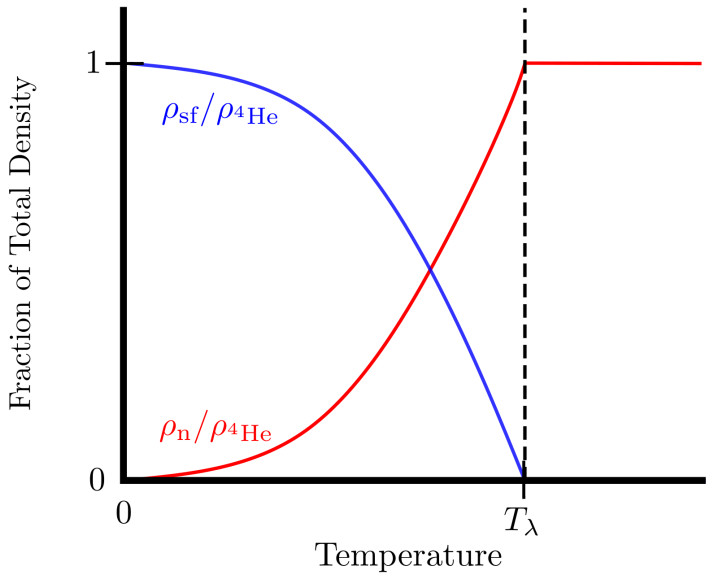

Figure 1.1: Qualitative plot of the temperature dependence of the density of the superfluid (ρ_{sf}, blue curve) and normal fluid (ρ_n, red curve) components of low-temperature helium as a fraction of the total density $\rho_{^4He}$.

supercurrent is possible due to an energy gap between the quantum ground state and the first excited state[20]. If the energy of the pairs is sufficient, they have enough momentum to jump the energy gap separating the ground and excited states and once again behave normally.

In a superfluid, however, no such energy gap exists. This is illustrated in the dispersion relation for ^{4}He, which can be seen in Fig. 1.2. There are no wave numbers for which excitations are impossible. The existence of superflow in superfluids is thus due to different mechanisms. The simplest is the Landau criterion, responsible for the Landau critical velocity v_L[1]. To derive v_L, consider an object of mass m passing through a superfluid with velocity $\mathbf{v}$. Suppose this object generates an excitation in the superfluid, with energy E_{exc} and momentum $\mathbf{p}_{exc}$. The generation of excitations must conserve momentum and energy

$$\frac{1}{2}mv^2 = \frac{1}{2}m(v')^2 + E_{exc} \tag{1.1}$$

$$m\mathbf{v} = m\mathbf{v}' + \mathbf{p}_{exc}, \tag{1.2}$$

where $\mathbf{v}'$ is the velocity of the projectile after the excitation is produced. Eq. (1.2)

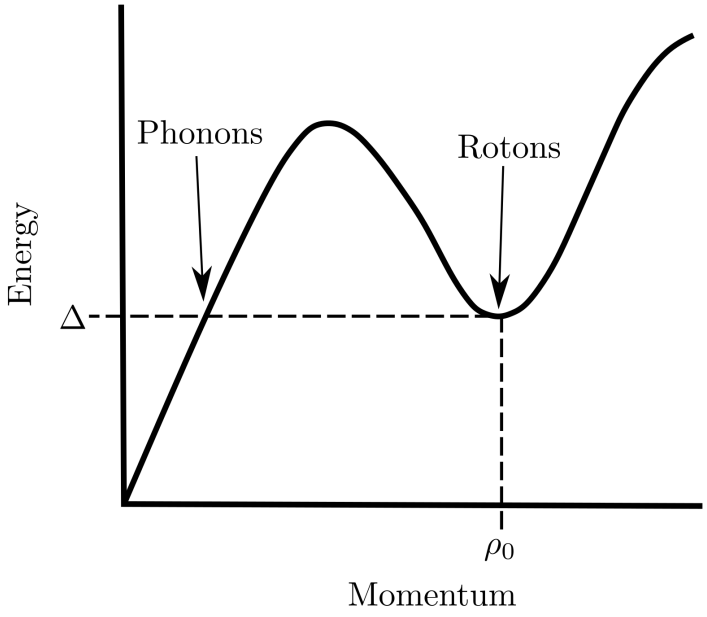

Figure 1.2: Qualitative plot of the dispersion relation for ^{4}He. Image adapted from Guénault[1].

yields $\mathbf{v}' = \mathbf{v} - \mathbf{p}_{\text{exc}}/m$. Eq. (1.1) then gives

$$\begin{aligned} &\frac{1}{2}mv^2 = \frac{1}{2}m\left|\mathbf{v} - \frac{\mathbf{p}_{\text{exc}}}{m}\right|^2 + E_{\text{exc}} = \frac{1}{2}mv^2 - \mathbf{p}_{\text{exc}}\cdot\mathbf{v} + \frac{p^2}{2m} + E_{\text{exc}} \\ &\Rightarrow E_{\text{exc}} = \mathbf{p}_{\text{exc}}\cdot\mathbf{v} - \frac{p^2}{2m} \leq p_{\text{exc}}v - \frac{p^2}{2m} \leq p_{\text{exc}}v \end{aligned} \tag{1.3}$$

Thus, the projectile velocity needed to produce this excitation must satisfy

$$v \geq \frac{E_{\text{exc}}}{p_{\text{exc}}}. \tag{1.4}$$

Assuming m is sufficiently large that $\dfrac{p^2}{2m}$ is negligible, the Landau critical velocity necessary to produce *any* excitations is[1]

$$v_{\text{L}} = \left(\frac{E_{\text{exc}}}{p_{\text{exc}}}\right)_{\text{min}}. \tag{1.5}$$

Although these calculations were done for a projectile moving through stationary fluid, this picture is equivalent to a moving fluid encountering a stationary object,

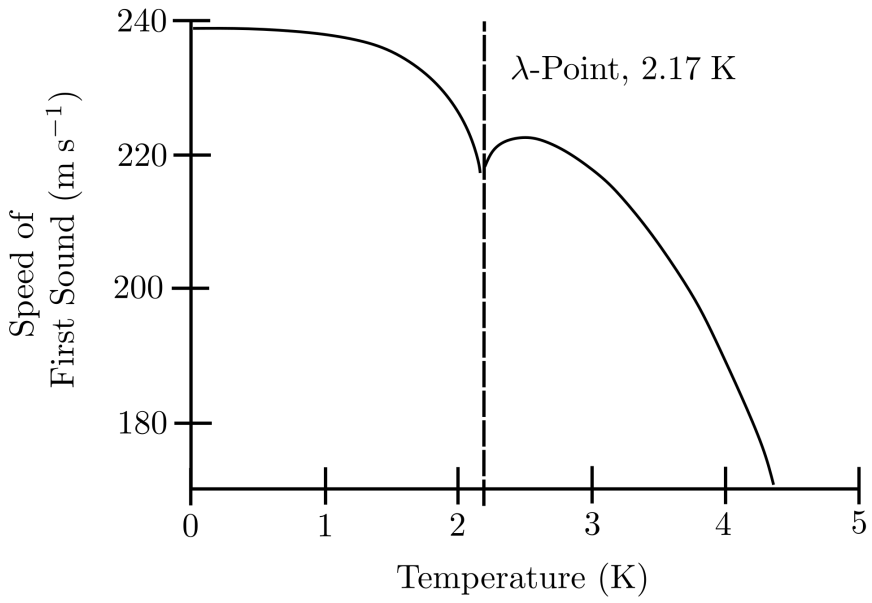

Figure 1.3: Approximate plot of the temperature dependence of the speed of first sound in ^{4}He. Image adapted from Atkins[2].

for example imperfections in an interface along which the fluid flows. Eq. (1.5) is therefore a general result.

The value of $\frac{E_{\text{exc}}}{p_{\text{exc}}}$ can be found from the dispersion relation. As illustrated in Fig. 1.2, there exist two regimes in the dispersion of ^{4}He. In the phonon regime, dispersion is caused by phonons travelling at the speed of sound c. The energy of excitations in this regime is thus $E_{\text{phonon}} = pc$, so[1]

$$\frac{E_{\text{exc}}}{p_{\text{exc}}} = c. \tag{1.6}$$

The speed of sound in He-II depends upon temperature as seen in Fig. 1.3, but will be between approximately 220 and 240 m s^{-1} in the superfluid phase. For larger momenta, the phonon regime gives way to the roton regime, with the energy of excitations given by[1]

$$E_{\text{roton}} = \Delta + \frac{(p - p_0)^2}{2m_{^4\text{He}}}, \tag{1.7}$$

where (p_0, Δ) is the location of the roton minimum marked in Fig. 1.2 and $m_{^4\text{He}}$ is the effective mass of a ^{4}He atom in the superfluid. The minimum of the ratio $\frac{E_{\text{exc}}}{p_{\text{exc}}}$

then occurs where

$$\frac{d(E_{\text{exc}}/p_{\text{exc}})}{dp} = \frac{d}{dp}\left(\frac{\Delta}{p} + \frac{(p-p_0)^2}{2m_{^4\text{He}}p}\right) = 0. \tag{1.8}$$

The momentum at which $\frac{E_{\text{exc}}}{p_{\text{exc}}}$ is minimised is thus

$$p_{\text{min}} = \sqrt{p_0^2 + 2m_{^4\text{He}}\Delta} \tag{1.9}$$

and therefore

$$\left(\frac{E_{\text{exc}}}{p_{\text{exc}}}\right)_{min} = \frac{\Delta}{\sqrt{p_0^2 + 2m_{^4\text{He}}\Delta}} + \frac{(\sqrt{p_0^2 + 2m_{^4\text{He}}\Delta} - p_0)^2}{2m_{^4\text{He}}\sqrt{p_0^2 + 2m_{^4\text{He}}\Delta}}. \tag{1.10}$$

In He-II, $p_0 \approx 2.1 \times 10^{-24}\,\text{kgm}\,\text{s}^{-1}$, $\Delta \approx 1.2 \times 10^{-22}\,\text{J}$, and $m_{^4\text{He}} \approx 6.6 \times 10^{-27}\,\text{kg}$[21], yielding $\frac{E_{\text{exc}}}{p_{\text{exc}}} \approx 53\,\text{m}\,\text{s}^{-1}$. Thus,

$$v_{\text{L}} = \text{min}\left\{\left(\frac{E}{p}\right)^{\text{phonon}}_{\text{min}}, \left(\frac{E}{p}\right)^{\text{roton}}_{\text{min}}\right\} = 53\,\text{m}\,\text{s}^{-1}. \tag{1.11}$$

In specific cases of superfluid flow far from an interface, most notably observations of ions travelling through a bulk of He-II[22] and molecules propelled through helium nanodroplets[23], the critical velocity is close to v_{L}. In many cases, however, experimental observations of the onset of dissipation in He-II suggest a far lower critical velocity. When superfluid flows through a pipe or other constriction, the critical velocity can be $0.5\,\text{m}\,\text{s}^{-1}$ or lower[24,25]. Vibrating tuning forks submerged in ^{4}He generally begin to experience drag at approximately $0.05\,\text{m}\,\text{s}^{-1}$[26]. Another dissipation mechanism thus operates at superfluid velocities lower than v_{L}. Rather than being mediated by phonons and rotons, dissipation in this regime occurs due to the generation of quantum vortices.

1.1.3 Quantum vortices

Vortices are common structures in classical fluids, consisting of fluid moving in a closed line about a central axis with velocity dependent upon the distance r from the axis. Typically, vortices are either irrotational, with velocity proportional to $\frac{1}{r}$; rigid-body, with velocity proportional to r; or, more commonly, some combination of rotational and irrotational flow. In viscous fluids dissipation is negligible in rigid-body rotation, such as that of a rotating bucket, but significant in irrotational systems, such as most free vortices, due to shear between regions of differing angular velocity.

Proposed by Feynman in 1955[27] and first observed by Vinen in 1961[28], quantum vortices are vortex lines similar to those in classical turbulence that carry quantized circulation. Quantum vortices are always irrotational, even when the normal component of a mixed superfluid-classical fluid system experiences rigid-body rotation. The existence and character of these excitations is a consequence of quantum condensation. Consider atoms of ^{4}He in the superfluid ground state. Since they form a Bose-Einstein condensate, they can be described by a single wavefunction; for simplicity, assume it is a free-particle wavefunction such that[1]

$$\Psi = C(\mathbf{r}, t)e^{i\tilde{\phi}(\mathbf{r},t)}, \tag{1.12}$$

where C is amplitude and $\tilde{\phi}$ is phase, both dependent upon space and time. Spatial contortions of a wavefunction correspond to the system's momentum, so the phase can be written as

$$\tilde{\phi} = \mathbf{k} \cdot \mathbf{r} = \frac{\mathbf{p} \cdot \mathbf{r}}{\hbar} = \frac{m_{^4\mathrm{He}}\mathbf{v}_{\mathrm{sf}} \cdot \mathbf{r}}{\hbar}, \tag{1.13}$$

where $\mathbf{k}$ is the wavevector, $\mathbf{r}$ is the position vector, $\mathbf{p}$ is momentum, $\mathbf{v}_{\mathrm{sf}}$ is the superfluid velocity, and $m_{^4\mathrm{He}}$ is the mass of a ^{4}He atom. Inverting this equation yields

$$\mathbf{v_{sf}} = \frac{\hbar}{m_{^4\mathrm{He}}} \bigtriangledown \tilde{\phi}. \tag{1.14}$$

Circulation is defined as the integral of the velocity along a closed line

$$\oint \mathbf{v_{sf}} \cdot d\boldsymbol{\ell} = \oint \frac{\hbar}{m_{^4\mathrm{He}}} \bigtriangledown \tilde{\phi} \cdot d\boldsymbol{\ell}. \tag{1.15}$$

If the fluid occupies a connected region, the wavefunction must obey periodic boundary conditions. Thus, the phase difference around any closed line must be an integer multiple of 2π, and the circulation must therefore be

$$\frac{h}{m_{^4\mathrm{He}}} n = n\kappa, \tag{1.16}$$

where κ is the circulation quantum and n is an integer. It should be noted that the derivation of v_{sf} accounts for only the fraction of the superfluid in the quantum ground state. However, the motion of atoms not in the ground state is expected to be entirely random, with the average net motion equal to that of the ground state. Eq. (1.14) is therefore a general result for the whole superfluid, if v_{sf} is taken to be the average net velocity. If the region is simply connected, n must be zero since the integral may be taken about an arbitrarily small line. However, if the region is multiply-connected, for example possessing a singularity around which the fluid circulates, this is not the case, and any integer is possible[29].

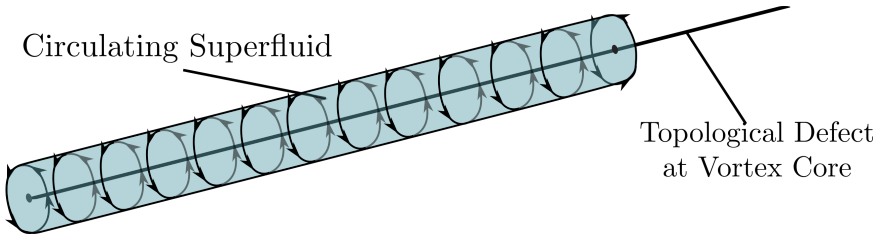

Figure 1.4: Qualitative diagram of a superfluid vortex filament.

In quantum vortices, this central singularity is provided by a topological defect in the fluid, a singularity in the velocity field forming a core with radius approximately equal to the inter-atomic spacing and typically no greater than 0.1 nm[3,30]. A qualitative depiction of a vortex filament can be found in Fig. 1.4.

Although any number of circulation quanta are possible, only single-quantum vortices are energetically favourable. To see this, consider a container with superfluid filled to a depth l and multiple parallel vortices with core radius ξ and average distance between vortices b. The kinetic energy per unit length of vortex $\varepsilon = E/l$ is then given by[20]

$$\varepsilon = \frac{1}{l} \iiint_V \frac{1}{2} \rho_{sf} v_{sf}^2 dV, \tag{1.17}$$

where ρ_{sf} is the superfluid mass density and the integral is over the average volume of fluid between two nearest-neighbour vortices. Thus,

$$\varepsilon = \frac{1}{2}\frac{1}{l} \int_\xi^b \int_0^{2\pi} \int_0^l \rho_{sf} \left(\frac{\kappa n}{2\pi r}\right)^2 r dz d\phi dr = \rho_{sf} \frac{\kappa^2}{4\pi} n^2 \ln\left(\frac{b}{\xi}\right). \tag{1.18}$$

Since energy is proportional to the square of the number of circulation quanta n, a two-quanta vortex would have four times the energy of a single-quantum vortex. It is therefore thermodynamically favourable for multi-quanta vortices to split into many single-quantum vortices.

The generation of quantum vortices can explain the very low experimentally observed critical velocity of ^{4}He, particularly when fluid flows through pipes, grids, or other narrow spaces, using an argument due to Feynman[31]. Consider superfluid flowing with velocity v out of a constriction of radius R into a bulk reservoir. Let the coordinate r be the radial distance from the central axis of the constriction, and z be the lateral distance from the end of the constriction. Consider a rectangular path C of length l in the $\hat{\mathbf{z}}$ direction with one edge at $r = 0$ and the parallel edge at $r = 2R$. As in a classical system, fluid flowing out of a constriction will "fan out", with fluid farther from the central axis moving slower than fluid closer to the centre.

Assume a simple model in which the fluid flows with velocity v in a "tube" of radius R extending in the $\hat{\mathbf{z}}$ direction from the end of the constriction, and is stationary elsewhere. This discontinuity in the velocity field will give rise to a series of vortices along the interface between the moving and stationary fluid. Assuming all the vortices have a single quantum of circulation, the net vortex velocity about C is

$$v_C = \oint_C \mathbf{v} \cdot d\mathbf{r} = nl\kappa, \tag{1.19}$$

where n is the number of vortices per unit length. In terms of the general velocity v of the superfluid, then,

$$n = \frac{v}{\kappa}. \tag{1.20}$$

The energy of the nucleated vortices per unit length of flow per unit time is then equal to the product of ε, n, and v

$$E_{\text{vort}} = \rho_{sf} \frac{\kappa^2}{4\pi} \ln\left(\frac{b}{\xi}\right)\left(\frac{v}{\kappa}\right) v = \frac{\rho_{sf}\kappa v^2}{4\pi} \ln\left(\frac{2R}{\xi}\right), \tag{1.21}$$

where the distance between vortices is assumed to be $2R$. The energy of the superfluid leaving the constriction per unit length per unit time is

$$E_{\text{sf}} = \frac{1}{2}\left(\rho_{sf} v^2\right) vR. \tag{1.22}$$

The energy of the turbulence E_{vort} must be equal to the energy of the flow creating it E_{sf}. Thus,

$$v = \frac{\kappa}{2\pi R} \ln\left(\frac{2R}{\xi}\right) \equiv v_c. \tag{1.23}$$

Eq. (1.23) is only an approximation, but suggests critical velocities far closer to those observed experimentally than does the Landau criterion. For a 67 µm pipe, such as that used in an experiment by Baehr *et al.*[32], Eq. (1.23) would suggest $v_c \approx 0.6\,\text{cm}\,\text{s}^{-1}$, compared with the experimental observation of $v_c \approx 1.5\,\text{cm}\,\text{s}^{-1}$.

The quantization of turbulence in superfluid is the primary reason for superfluid's utility as a "toy model" for classical turbulence. Individual quantum vortices may be trapped and probed, and the evolution of these structures is much easier to track experimentally and explain mathematically than the many eddies of arbitrary size that comprise classical turbulence[33].

1.1.4 Vortex reconnection

When two vortices, or two segments of the same vortex, move sufficiently close, they often reconnect with each other, a process illustrated in Fig. 1.5. Both vortex lines

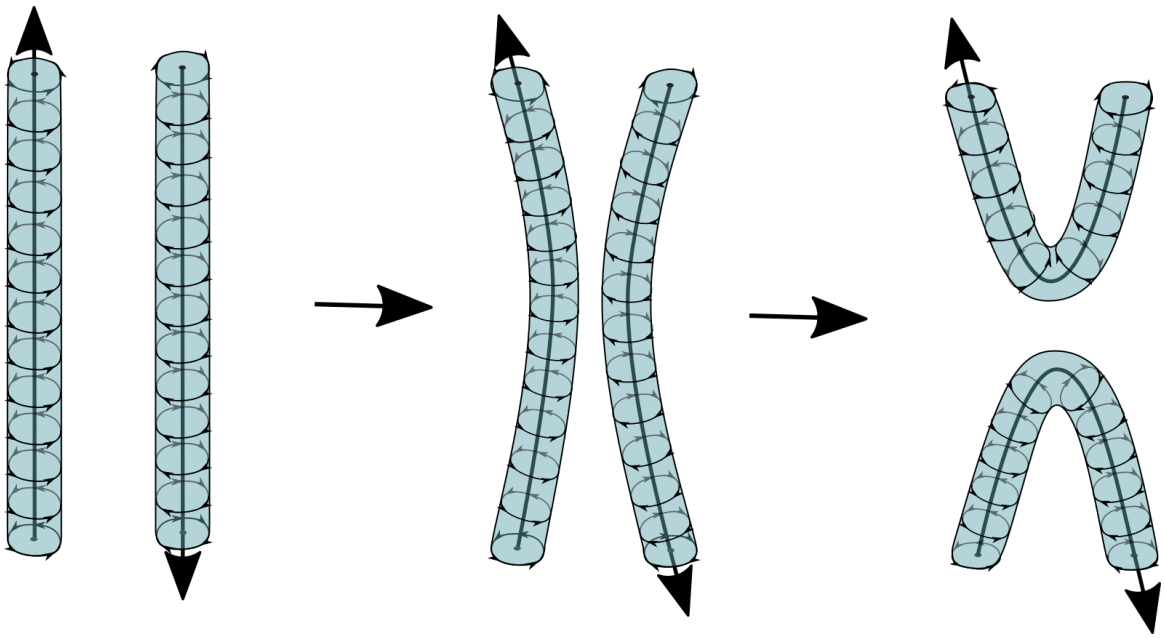

Figure 1.5: Qualitative depiction of the vortex reconnection process.

will split, and the ends will reconnect to the ends of the other vortex. Reconnection events occur most readily for antiparallel vortices, in which the axes of rotation point opposite directions at the point of closest approach. Numerical simulations have demonstrated that even vortices with perpendicular axes of rotation can reconnect if sufficiently close, however[34].

This process is known to occur in classical vortices, being a prediction of the Navier-Stokes equations[35] and an experimentally observed phenomenon[36]. In superfluid, vortex reconnection has been studied numerically as a prediction of both the Biot-Savart law[37,38] and Gross-Pitaevskii equation[39–42], as well as experimentally[43]. Numeric studies using the Gross-Pitaevskii model have additionally predicted that reconnections will result in the emission of a phonon[44].

Notably, after reconnection, the resultant vortices will have "kinks", as seen in Fig. 1.5. These kinks cannot exist in equilibrium and will relax, becoming smooth curves. When they do, they perturb the entire vortex line, creating propagating helical displacements called Kelvin waves[45].

1.1.5 Kelvin waves

Kelvin waves were first proposed by Lord Kelvin to describe waves in water[46], and are widely used in classical fluid dynamics to model oceanic[47] and atmospheric[48] gravity

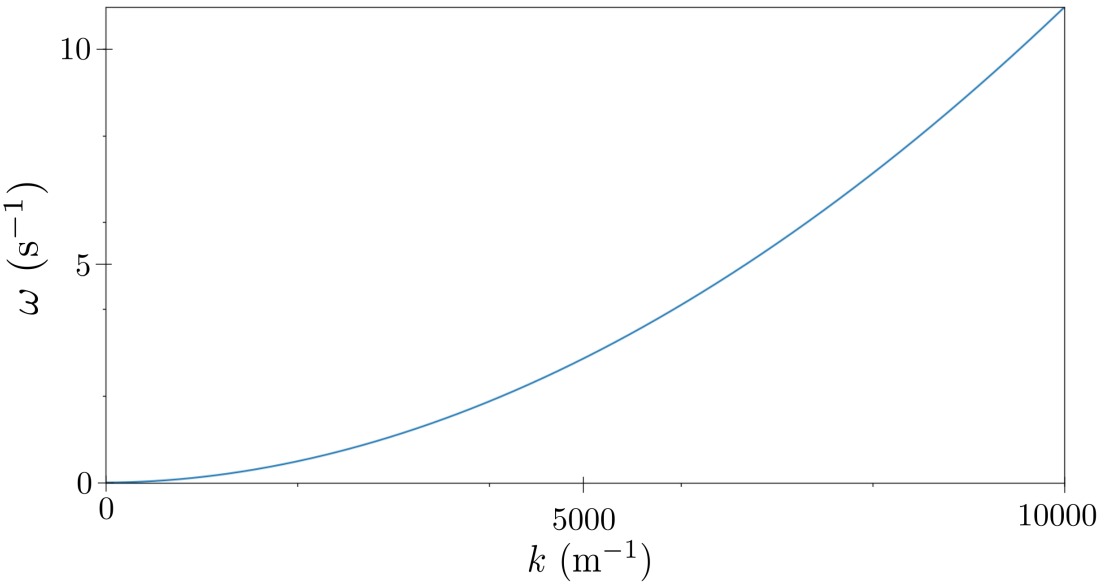

Figure 1.6: Plot of the dispersion relation for kelvons on a quantum vortex in ^{4}He, given by Eq. (1.24).

waves. In superfluids and non-superfluid BECs, they are applied to waves travelling along vortex filaments[45], where they behave as quasiparticles called kelvons[20]. Kelvin waves admit the dispersion relation[29]

$$\omega = \frac{\kappa k^2}{4\pi} \ln\left(\frac{1}{k\xi}\right), \tag{1.24}$$

where k is the wavenumber. A plot of Eq. (1.24) can be seen in Fig. 1.6. Direct experimental observation of Kelvin waves on a single vortex in a BEC of rubidium was achieved by Bretin *et al.*[49,50], and observation of Kelvin waves on a superfluid ^{4}He vortex was achieved by Fonda *et al.* by injecting tracer molecules into vortex lines[51]. Kelvin waves are believed to play a fundamental role in the dissipation of turbulent energy at the smallest of length scales in superfluids.

1.2 Energy dissipation

Although a characteristic of superfluid is its ability to flow without viscosity, quantum vortices do dissipate energy. At high temperatures and large length scales the dissipation mechanisms mirror those of a classical fluid. At lengths smaller than

the average distance between vortices, however, different processes are believed to take over, the precise nature of which has not yet been fully explored.

1.2.1 Dissipation in classical turbulence

In a classical fluid, turbulence is dissipated via the Kolmogorov cascade, in which energy is transferred to progressively smaller length scales as large vortices break apart and reconnect into many smaller vortices[52]. The kinetic energy stored in the vortices is largely conserved until the Kolmogorov length scale is reached, at which point energy is ultimately dissipated as heat from friction between fluid molecules. Length scales between the characteristic length - the length scales of the initial turbulent eddies - and the Kolmogorov scale are known as the inertial range[11].

The Kolmogorov cascade is characterised by its energy spectrum[53]. If k is the wavenumber of a turbulent excitation, then the energy spectrum $E(k)$ gives the average energy per unit mass of excitations with wavenumber k. The spectrum was derived by Kolmogorov[54] and is known to be

$$E(k) = C\epsilon^{2/3}k^{-5/3}, \tag{1.25}$$

where ϵ is the rate at which energy per unit mass is transferred to smaller length scales and C is a constant[53]. Since energy is constantly flowing down the cascade, the rate of energy transfer in the inertial range must be equal to the rate of dissipation on the Kolmogorov scale. Assuming that the boundary of the region containing the turbulent vorticity experiences viscous stress[52] and that the turbulence is homogeneous and isotropic, the dissipation rate can be shown to be[53]

$$\epsilon = \nu\langle\omega^2\rangle, \tag{1.26}$$

where ν is viscosity, $\omega = \bigtriangledown \times \mathbf{v}$ is vorticity, and $\langle\omega^2\rangle$ is the mean square vorticity.

1.2.2 Dissipation in quantum turbulence

The Kolmogorov cascade can be seen in quantum vortices. At large length scales, individual vortices become difficult to resolve and the energy cascade is dominated by their collective behaviour, which mirrors classical turbulence[55]. Similar to a classical fluid, large superfluid vortices will split and reconnect to form many shorter vortex lines. At small length scales, however, the superfluid cascade diverges from the classical[45]. The small-scale energy cascade is dominated by Kelvin waves, which ultimately dissipate energy into the surrounding fluid[55].

The available mechanisms by which energy can be transferred to the environment are restricted by the quantum nature of superfluid vortices. At high temperatures close

to the phase boundary, the normal fluid fraction is much larger than the superfluid fraction. Dissipation at very small scales is then believed to be mediated by classical, viscous dissipation in the normal fluid component[55].

However, at lower temperatures, particularly below about 1 K, the normal fluid fraction is negligible. Vortex energy cannot be lost by "slowing down", reducing circulation, as circulation cannot fall below its minimum value of $h/m_{^4\mathrm{He}}$ until the vortex fully dissipates. Energy can, however, be reduced by a reduction of the total length of vortex lines. Length contraction occurs during reconnection events, in which two lengths of vortex split and reconnect with each other. The total length of the resultant vortices is slightly smaller than their initial lengths. Some of the energy associated with the length difference is radiated as a phonon during reconnection[44]. The remainder is transferred to Kelvin wave excitations of the child and parent vortices[45]. Kelvin waves follow a process analogous to the Kolmogorov cascade, with wavelength declining over time[55]. As in the classical cascade, the large-wavelength Kelvin waves experience minimal dissipation, instead simply transferring energy to smaller length scales. Eventually, however, Kelvin waves are generated with sufficiently high frequency to begin to radiate phonons, completing the transfer of energy back to the environment[56,57]. This process is known as the Kelvin wave cascade to distinguish it from the long-length-scale Kolmogorov cascade.

Recent work suggests the Kelvin cascade may be complemented by further self-reconnections as Kelvin wavelength decreases. The reduction in wavelength during the cascade necessarily means local curvature of the vortex line will increase. Eventually, local curvature will increase to the point that loops form in the vortex line, which could then break off in a self-reconnection event. The parent and child vortices then continue the cascade to ever-smaller length scales until all turbulent energy has been converted to phonons[45].

The spectrum of the Kelvin wave cascade is an open problem. Two competing theories have been put forward to describe it. The first, developed by Kozik and Svistunov[58], assumes local six-wave interaction to derive the energy spectrum[58,59]

$$E(k) = C_6 \kappa^{7/5} \epsilon^{1/5} k^{-7/5}, \tag{1.27}$$

where C_6 is a dimensionless constant, κ is the circulation quantum, and ϵ is the energy flux. It was later suggested by L'vov that the locality assumption used to derive Eq. (1.27) was invalid[60] and, using local four-wave interaction, a different spectrum was derived by L'vov and Nazarenko[59,60]

$$E(k) = C_4 \kappa^{5/3} \epsilon^{1/5} \Psi^{-2/3} k^{-5/3}, \tag{1.28}$$

where C_4 is a dimensionless constant and Ψ is

$$\Psi = \frac{2}{\gamma} \int_{1/l_v} k^2 n(k) dk, \tag{1.29}$$

where l_v is the inter-vortex spacing and $n(k)$ is the action density for a wave with wavenumber k. There has been, and remains, debate regarding which formulation is more accurate, although there is growing consensus in favour of the L'vov-Nazarenko model (Eq. (1.28)) based on numerical studies[59,61–68].

It should be noted that while the picture of the Kelvin wave cascade is supported by theory[56] and numerical studies[44,69], there has not yet been a direct observation of cascading Kelvin waves, phonon emission from reconnection, or Kelvin-wave-induced self-reconnection[68]. A simple and reliable means of experimentally probing Kelvin wave dynamics on individual vortices would be an important step towards better understanding the Kelvin cascade. Vortex trapping using nanoelectromechanical resonators could provide such a means.

1.3 Nanoelectromechanical resonators

A common tool used to probe turbulence and other phenomena in superfluids is the nanoelectromechanical resonator. Two of the most common resonator layouts are doubly-clamped beams (Fig. 1.7a) and tuning forks (Fig. 1.7b). In this study, a tuning fork is used to generate vortices, while a doubly-clamped beam is used to probe them. When a vortex moving through the fluid comes into contact with the beam of the resonator, there is a chance that it may become "trapped", with circulation enveloping some or all of the beam and the ends of the vortex line pinned to either the resonator clamps or the walls of the sample cell. A "trapped" state alters the behaviour of the resonator, and by analysing these changes significant information about the vortex can be inferred. An accurate model of the behaviour of the doubly-clamped beam is necessary to quantify the changes, which often result in nonlinearity. The Duffing model of a nonlinear oscillator provides a useful description of the beam resonator used in this study.

1.3.1 Linear model

In the absence of mechanical or superfluid-originated nonlinear forces, the doubly-clamped beam resonator may be modelled as a simple driven-damped linear oscillator with flexural modes. Assuming the sole degree of freedom is the displacement of the centre of the beam $x(t)$, the equation of motion is

$$x'' + \zeta x' + \omega_0^2 x = \frac{1}{2} f \left(e^{i\omega t} + e^{-i\omega t} \right), \tag{1.30}$$

where ω_0 is the resonant frequency of the oscillator; ζ is the linear drag coefficient, also known as the damping ratio; $f = F/m$ is the magnitude of the drive force

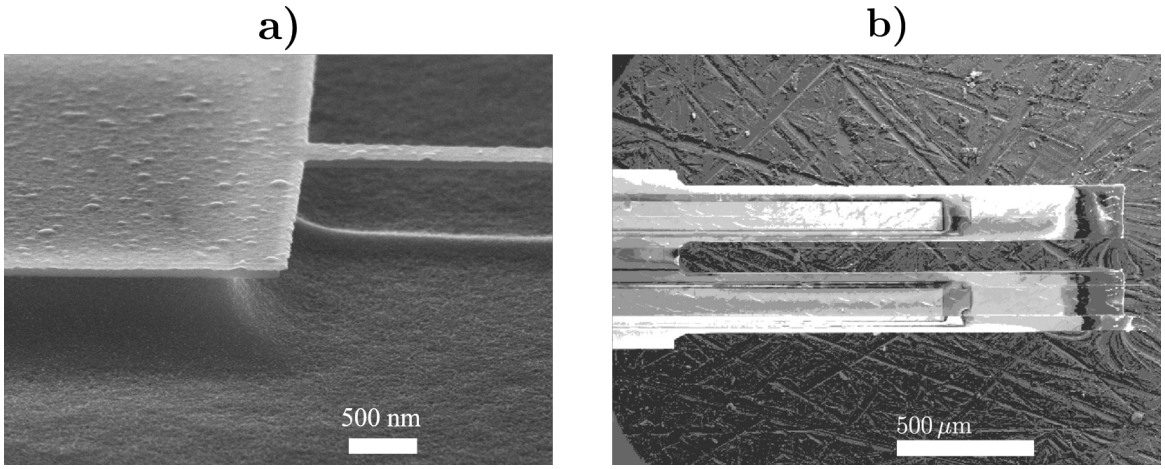

Figure 1.7: Devices used to generate and trap vortices. a) is an SEM image of the doubly-clamped beam, zoomed-in on one of the clamps. This image was used to estimate the cross-sectional dimensions of the beam extending towards the right of the image (130 nm by 200 nm), as well as the distance from the beam to the substrate (1 µm). b) is an SEM image of a tuning fork. The tuning fork shown is a sister sample of the device used in this study, with very similar structure.

normalised to the the effective mass m of the oscillator; and ω is the drive frequency. By introducing the dimensionless time $\tilde{t} = \omega_0 t$, the equation can be rewritten

$$x''_{\tilde{t}} + \tilde{\zeta} x'_{\tilde{t}} + x = \frac{1}{2}\frac{f}{\omega_0^2}\left(e^{i\tilde{\omega}\tilde{t}} + e^{-i\tilde{\omega}\tilde{t}}\right), \tag{1.31}$$

where $\tilde{\omega} = \dfrac{\omega}{\omega_0}$ and $\tilde{\zeta} = \dfrac{\zeta}{\omega_0}$ are the dimensionless drive frequency and drag coefficient, respectively. The general solution of this equation can be written

$$x = \frac{1}{2}\left(x_0 e^{i\tilde{\omega}\tilde{t}} + x_0^* e^{-i\tilde{\omega}\tilde{t}}\right), \tag{1.32}$$

where x_0 is the complex amplitude of oscillation. By using this trial function one can obtain the frequency response of the resonator

$$x_0^2 = \left(\frac{f}{\omega_0^2}\right)^2 \frac{1}{\left(\tilde{\omega}^2 - 1\right)^2 + \tilde{\omega}^2\tilde{\zeta}^2}. \tag{1.33}$$

Equation (1.33) is a Lorentzian function relating the amplitude of oscillation to the drive frequency, and has a peak about the resonant frequency $\tilde{\omega} = 1$. Plots of Equation (1.33) for various values of $\tilde{\zeta}$ can be seen in Fig. 1.8. Note that the quality factor Q of the resonator is equal to $Q = \tilde{\zeta}^{-1}$.

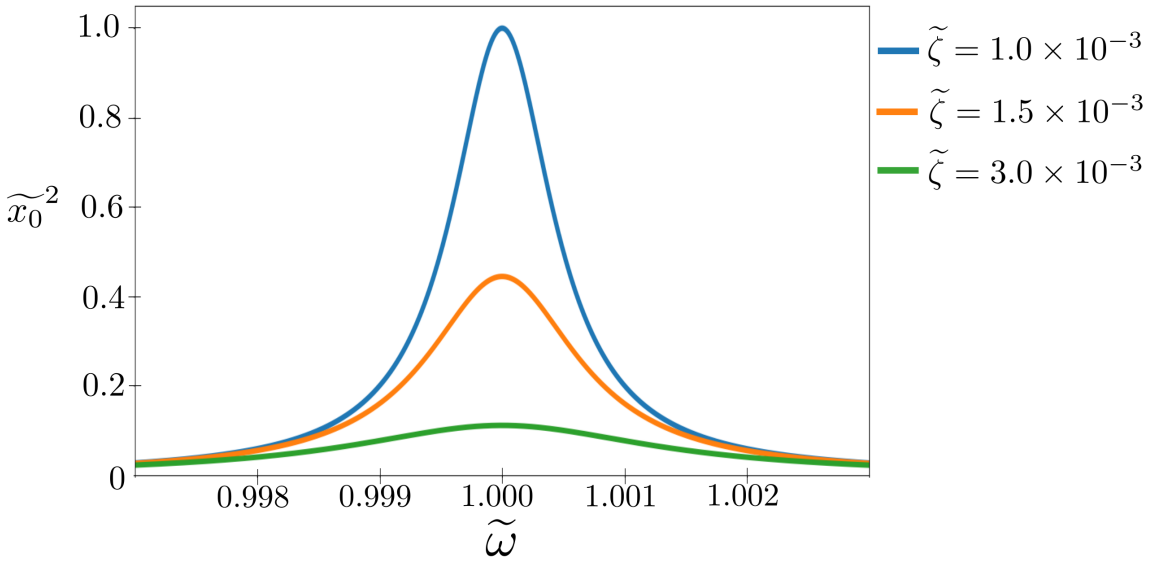

Figure 1.8: Frequency response of a linear driven-damped oscillator (Eq. (1.33)) with different values of the dimensionless linear drag coefficient $\widetilde{\zeta}$. The dimensionless amplitude $\widetilde{x_0}$ is equal to $x_0\omega_0^2/f$, and the dimensionless frequency $\tilde{\omega}$ is equal to ω/ω_0.

1.3.2 Duffing force

This description is not sufficient, however, when nonlinear effects become significant. Nonlinearities may originate internally, for example mechanical nonlinearities due to strain in the beam, or externally, for example due to interactions with trapped vortices. In the absence of interactions with the superfluid, the beam resonator used in this study is expected to develop a Duffing-type nonlinearity of the form αx^3 at sufficiently high oscillation amplitudes. This additional force functions as a nonlinear restoring force. While α can be positive, thereby "hardening" the resonator, or negative, "softening" the resonator, the intrinsic, mechanical nonlinearity will result in a positive α as the beam resists stretching when the amplitude of oscillation becomes sufficiently large, of the same order of magnitude as the width of the beam[70]. Multiple physical effects can give rise to a Duffing-type force, depending upon the arrangement of the resonator and the environment. See Chapter A for a derivation of the Duffing force due to resistance by the beam's material to stretching, as well as an estimation of the intrinsic Duffing parameter for our doubly-clamped beam. Interaction with a partially-trapped vortex may also be modelled as a Duffing force, though with a negative α. This will be discussed further in Chapter 4.

1.3.3 Duffing model

Taking as a given the existence of a Duffing force, the equation of motion for a driven-damped oscillator becomes

$$x'' + \zeta x' + \omega_0^2 x + \alpha x^3 = \frac{1}{2} f \left(e^{i\omega t} + e^{-i\omega t} \right). \tag{1.34}$$

A general closed form solution for Eq. (1.34) does not exist. However, provided the quality factor of the resonator is sufficiently large and the amplitude of oscillation is sufficiently small, secular perturbation theory may be applied to extract an approximate frequency response, following a derivation by Lifshitz and Cross[70].

Dimensionless variables $\tilde{t} = \omega_0 t$ and $\tilde{x} = x\sqrt{\frac{\alpha}{\omega_0^2}}$ are introduced for time and displacement, respectively. Normalisation of all terms of Eq. (1.34) yields the scaled equation of motion

$$\tilde{x}_{\tilde{t}}'' + \tilde{\zeta}\tilde{x}_{\tilde{t}}' + \tilde{x} + \tilde{x}^3 = \frac{1}{2}\tilde{f}\left(e^{i\tilde{\omega}\tilde{t}} + e^{-i\tilde{\omega}\tilde{t}} \right), \tag{1.35}$$

where $\tilde{f} = \frac{f\sqrt{\alpha}}{\omega_0^3}$. Provided the linear drag coefficient and displacement are sufficiently small such that $\tilde{\zeta} \ll 1$ and $O(\tilde{x}) = O\left(\tilde{\zeta}^{1/2}\right)$, damping may be considered a perturbation. From the linear harmonic oscillator, it must be that $\tilde{x} \propto \tilde{f}\tilde{\zeta}^{-1}$ and thus $O(\tilde{f}) = O(\tilde{\zeta}^{\frac{3}{2}})$. Drive force may therefore be considered a perturbation as well.

Define a new, further-scaled drive amplitude g such that $\tilde{f} = \tilde{\zeta}^{\frac{3}{2}} g$. This analysis concerns frequencies in a range of order $\tilde{\zeta}$ about the resonant frequency $\tilde{\omega} = 1$. It is therefore convenient to introduce a new frequency Ω such that $\tilde{\omega} = 1 + \tilde{\zeta}\Omega$. Eq. (1.35) then becomes

$$\tilde{x}_{\tilde{t}}'' + \tilde{\zeta}\tilde{x}_{\tilde{t}}' + \tilde{x} + \tilde{x}^3 = \frac{1}{2} g \tilde{\zeta}^{\frac{3}{2}} \left(e^{i(1+\tilde{\zeta}\Omega)\tilde{t}} + e^{-i(1+\tilde{\zeta}\Omega)\tilde{t}} \right). \tag{1.36}$$

Eq. (1.36) can be solved by using the ansatz

$$\tilde{x}(\tilde{t}) = \frac{1}{2}\tilde{\zeta}^{\frac{1}{2}} \left(A(\tau) e^{i\tilde{t}} + \text{c.c.} \right) + \tilde{\zeta}^{\frac{3}{2}} y(\tilde{t}) + O(\tilde{\zeta}^{\frac{5}{2}}), \tag{1.37}$$

where $A(\tau)$ is the time-varying complex amplitude of oscillation of the resonator, $\tau = \tilde{\zeta}\tilde{t}$, and $y(\tilde{t})$ is the first-order perturbative correction. Note that the first term is the ansatz for a simple harmonic oscillator in scaled units. Inserting Eq. (1.37) into Eq. (1.36) and extracting only terms of order $\tilde{\zeta}^{3/2}$ yields the first-order perturbative correction

$$\tilde{y}_{\tilde{t}}'' + y(\tilde{t}) = \frac{1}{2} \underbrace{\left(-2iA_\tau' - iA - \frac{3}{4}|A|^2 A + g e^{i\tilde{\zeta}\Omega\tilde{t}} \right)}_{=0} e^{i\tilde{t}} + \frac{1}{8} A^3 e^{3i\tilde{t}} + \text{c.c.} \tag{1.38}$$

The terms multiplied by $e^{\pm i\tilde{t}}$ are the secular terms and act as an effective drive force at exactly the resonant frequency. If the first-order correction does not diverge, it must be that these terms sum to zero. This gives a differential equation in terms of the complex amplitude $A(\tau)$[1]

$$2iA'_\tau(\tau) + iA(\tau) + \frac{3}{4}|A(\tau)|^2 A(\tau) = ge^{i\Omega\tau}. \tag{1.39}$$

A good ansatz is harmonic motion at frequency Ω

$$A(\tau) = ae^{i\tau\Omega} = |a|e^{i\varphi}e^{i\Omega\tau}, \tag{1.40}$$

where φ is the phase of oscillation. Substituting Eq. (1.40) into Eq. (1.39) yields an algebraic equation for the amplitude of oscillation a

$$a = \frac{g}{i + \frac{3}{4}|a|^2 - 2\Omega}. \tag{1.41}$$

The real part of a can be found by multiplying Eq. (1.41) by a^*, yielding an implicit formula for the frequency response of the resonator

$$|a|^2 = \frac{g^2}{\left(\frac{3}{4}|a|^2 - 2\Omega\right)^2 + 1}, \tag{1.42}$$

or, in unscaled units

$$|x_0|^2 = \left(\frac{f}{\omega_0^2}\right)^2 \frac{1}{\left(2(\tilde{\omega}-1) - \frac{3}{4}\frac{|x_0|^2\alpha}{\omega_0^2}\right)^2 + \left(\frac{\zeta}{\omega_0}\right)^2}. \tag{1.43}$$

The phase can be found by inserting $a = |a|e^{i\varphi}$ into Eq. (1.41) and solving for $g/|a|$

$$\begin{aligned}\frac{g}{|a|} = &\left(\frac{3}{4}|a|^2 - 2\Omega\right)\cos\varphi - \sin\varphi \\ &+ i\left[\left(\frac{3}{4}|a|^2 - 2\Omega\right)\sin\varphi + \cos\varphi\right].\end{aligned} \tag{1.44}$$

The quantity $g/|a|$ must be real, so the imaginary terms must sum to zero. This yields a formula for φ

$$\tan\varphi = \frac{1}{2\Omega - \frac{3}{4}|a|^2}, \tag{1.45}$$

[1]Complex conjugate terms provide a similar equation.

or, in unscaled units

$$\tan\varphi = \frac{\dfrac{\zeta}{\omega_0}}{2(\tilde{\omega}-1) - \dfrac{3}{4}\dfrac{|x_0|^2\alpha}{\omega_0^2}}. \tag{1.46}$$

The time-varying displacement is thus the simple harmonic

$$x(t) = x_0\cos(\omega t + \varphi). \tag{1.47}$$

Eq. (1.43) may be further rewritten in terms of dimensionless parameters as

$$\widetilde{x}_0^2 = \frac{1}{\left(2(\widetilde{\omega}-1) - \dfrac{3}{4}\widetilde{\alpha}\widetilde{x}_0^2\right)^2 + \widetilde{\zeta}^2}, \tag{1.48}$$

where the dimensionless amplitude of oscillation $\widetilde{x}_0$ is

$$\widetilde{x}_0 = \frac{\omega_0^2 x_0}{f}, \tag{1.49}$$

and the dimensionless Duffing parameter $\widetilde{\alpha}$ is

$$\widetilde{\alpha} = \frac{\alpha f^2}{\omega_0^6}. \tag{1.50}$$

Eq. (1.43) is a "skewed" Lorentzian, similar to Fig. 1.8 with the resonant peak "pulled" towards either higher or lower frequencies. The direction of asymmetry is determined by the sign of α; a negative Duffing coefficient pulls the maximum amplitude of oscillation toward frequencies lower than the natural resonant frequency ω_0 (softening the resonator), and a positive Duffing coefficient pulls the maximum amplitude towards frequencies higher than ω_0 (hardening the resonator). The degree of asymmetry is determined by the magnitude of α, with higher magnitudes pulling the maximum amplitude further from ω_0. The effect of $\widetilde{\alpha}$ on the qualitative behaviour of Eq. (1.48) can be seen in Fig. 1.9

Eq. (1.43) provides an implicit relationship between the maximum amplitude of oscillation of the resonator x_0 and drive frequency ω, which can be fitted to experimental data with the Duffing parameter α, resonant frequency ω_0, drive force f, and linear drag ζ free parameters.

If nonlinear effects are sufficiently strong, a region of bistability may emerge, as seen in Fig. 1.9 when $\widetilde{\alpha} = \pm 7$. This is a prominent feature of experimental observations of nonlinear NEMS. Within this interval, bounded by two bifurcation points ω^+ and ω^-, there exist two stable and one unstable solutions to Eq. (1.48).

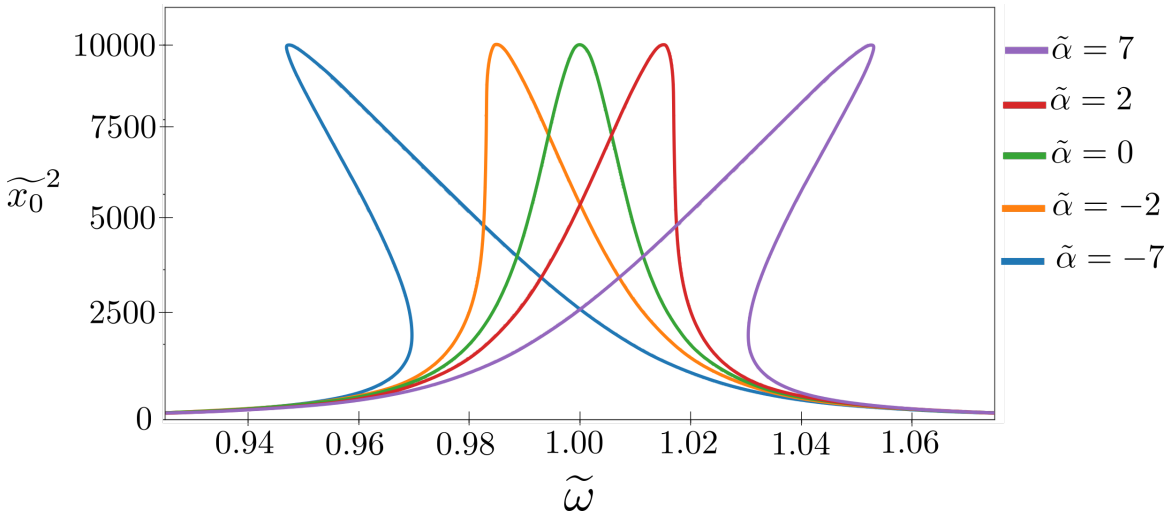

Figure 1.9: Plots of Eq. (1.48) with different values of the dimensionless Duffing parameter $\widetilde{\alpha}$. The dimensionless amplitude $\widetilde{x_0}$ is equal to $\omega_0^2 x_0/f$, and the dimensionless frequency $\tilde{\omega}$ is equal to ω/ω_0.

Both the existence and location of the bifurcation points, and thus the region of bistability, can be determined from Eq. (1.42). Since the bifurcation points are local extrema of the inverse amplitude function $(|a|^2)^{-1}(\Omega)$, they occur where $d\Omega/d|a|^2 = 0$. Taking a derivative of Eq. (1.42) with respect to Ω yields

$$\begin{aligned} &\frac{d|a|^2}{d\Omega}\left[-\frac{27}{64}|a|^4 - \frac{3}{2}\Omega|a|^2 + \frac{1}{4} + \Omega^2\right] = \frac{3}{4}|a|^4 - 2\Omega|a|^2 \\ &\Rightarrow \frac{27}{64}|a|^4 - \frac{3}{2}\Omega|a|^2 + \frac{1}{4} + \Omega^2 = \frac{d\Omega}{d|a|^2}\left[\frac{3}{4}|a|^4 - 2\Omega|a|^2\right]. \end{aligned} \tag{1.51}$$

Setting $d\Omega/d|a|^2 = 0$ means the right hand side of this equation is equal to zero, leaving a quadratic equation in Ω

$$\frac{27}{64}|a|^4 - \frac{3}{2}\Omega|a|^2 + \frac{1}{4} + \Omega^2 = 0 \tag{1.52}$$

which has solutions

$$\Omega^{\pm} = \frac{3}{4}|a|^2 \pm \frac{1}{2}\sqrt{\frac{9}{16}|a|^4 - 1}, \tag{1.53}$$

or, in unscaled units,

$$\omega^{\pm} = \omega_0 + \frac{3}{4}\frac{|x_0|^2\alpha}{\omega_0} \pm \frac{1}{2}\sqrt{\left(\frac{3}{4}\frac{|x_0|^2\alpha}{\omega_0}\right)^2 - \zeta^2}. \tag{1.54}$$

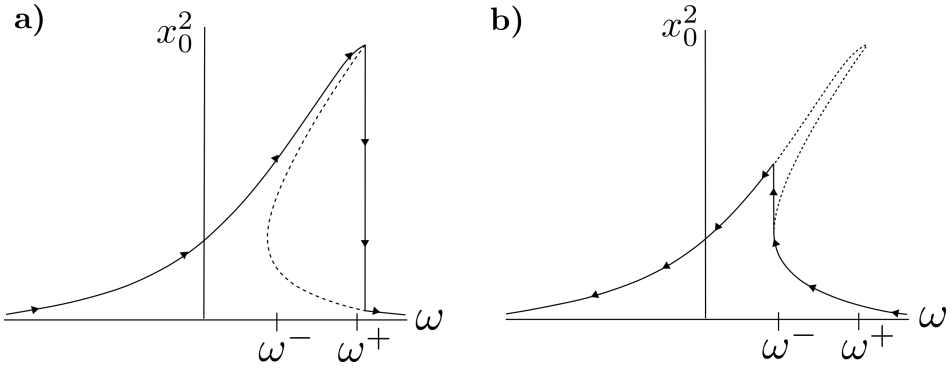

Figure 1.10: Hysteresis in the response of a Duffing oscillator exhibiting bistability during a) a drive frequency upsweep and b) a drive frequency downsweep.

Thus, the bifurcation points appear if and only if $\frac{3}{4}\frac{|x_0|^2\alpha}{\omega_0} > 1$, and are located at the corresponding frequencies ω^+ and ω^-. In Fig. 1.9, when $|\widetilde{\alpha}| < 2$ this is not the case. The birfurcation frequencies are complex, so there is no bistable region. When $|\widetilde{\alpha}| = 7$, however, Eq. (1.54) has two real solutions, and therefore a bistable region exists.

Bistability is a source of hysteresis in drive frequency sweeps of the resonator, as seen in Fig. 1.10. During drive frequency upsweeps (Fig. 1.10a) the system will remain on the upper (if $\alpha > 0$) or lower (if $\alpha < 0$) branches until reaching the second bifurcation point ω^+. The system will then make a discontinuous jump to the other branch, with resonator response decreasing (if $\alpha > 0$) or increasing (if $\alpha < 0$) suddenly and dramatically before decaying smoothly as drive frequency is further increased. During a drive frequency downsweep (Fig. 1.10b) the opposite will happen, with the discontinuous jump at the first bifurcation point ω^-. In practice, these jumps will typically happen at frequencies slightly lower than ω^+ and slightly higher than ω^- due to thermal noise pushing the system to the other branch prematurely.

The existence of bifurcation points give NEMS potential utility as highly sensitive sensors and detectors of quantum behaviour. For the former application, operating a resonator near one of the bifurcation points will allow a very small change in drive frequency, or any parameter which determines the location of the bifurcation points, to produce a strong and easily detectable change in response so long as noise can be sufficiently controlled for. For the latter application, the drive frequency and other parameters may be tuned so that thermal noise is insufficient to force the system to jump branches if the resonator is behaving classically, but if the resonator is behaving quantum mechanically it may tunnel between states with relative ease. This provides a means of determining whether the system is obeying classical or quantum rules[70].

The remainder of this work is laid out as follows: Chapter 2 will detail the

experimental setup and procedures used to trap vortices and probe their behaviour. Chapter 3 will present an analysis of the experimental data and argue for the existence of several mechanisms by which Kelvin waves on individual vortices modify the behaviour of our nanoelectromechanical resonator. Chapter 4 will present the results of fitting the driven-damped Duffing oscillator solution (Eq. (1.43)) to experimental data and briefly outline possible physical mechanisms that may be responsible for observed trends. Finally, Chapter 5 will provide a summary of the results, their utility in the broader drive to better understand superfluid turbulence, and potential next steps in this line of inquiry.

Chapter 2

Experiment

Experiments are conducted in a brass sample cell filled with high-purity ^{4}He, thermally connected to the mixing chamber of a cryogen-free dilution refrigerator. A pressure of approximately 0.8 bar and temperature of 12 mK is maintained in the sample cell. At this temperature and pressure the normal fluid component of the He-II is very small compared to the superfluid component, and the system can be well approximated as a pure superfluid. Two nanoelectromechanical resonators are present in the sample cell: a tuning fork and a doubly-clamped beam-type resonator. A diagram of the experimental setup can be seen in Fig. 2.1. Vortices generated by the tuning fork will travel in a random direction away from it. Some of these vortices will collide with the nearby beam resonator, and will occasionally become trapped by it. These trapped vortices alter the behaviour of the beam resonator, and the effect they have on the device's response can be used to infer the behaviour of the vortices themselves.

2.1 Tuning fork theory and operation

A quartz piezoelectric tuning fork, hereafter referred to as the "fork", is used to generate turbulence. The fork is actuated using the reverse piezoelectric effect, via an RF voltage signal applied at the fork's resonant frequency. The voltage is applied to electrodes on each prong, causing the quartz to expand and contract and thereby actuating the device. Assuming flexural modes of oscillation dominate torsional modes in the tuning fork, the drive force F applied to the fork is directly proportional to the voltage V applied to electrodes mounted on each quartz prong via

$$F = \frac{a_f V}{2}, \tag{2.1}$$

where a_f is the fork constant, determined by the geometry of the device as

$$a_f = 3d_{11}Ewh/l, \tag{2.2}$$

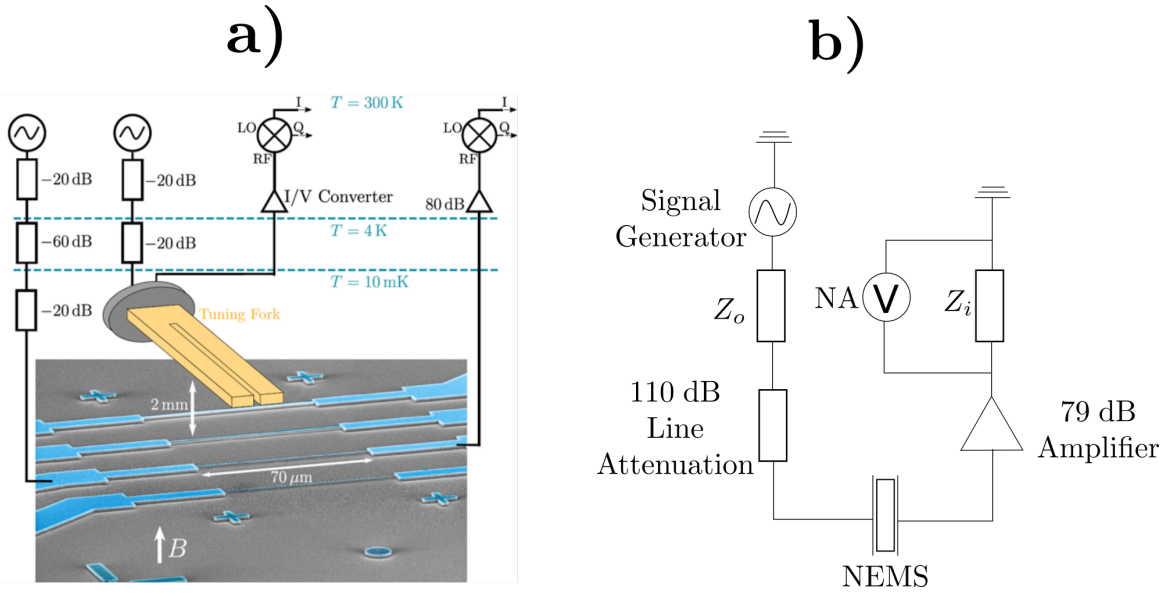

Figure 2.1: Schematic of the experimental setup used for real-time detection of quantized vortices. The overall setup is shown in a): a tuning fork generates quantum turbulence, while a 70 µm-long nanomechanical beam suspended 1 µm above the substrate is used as a detector. The beam and fork are driven by vector network analysers or signal generators through several stages of attenuation at different temperatures. The beam's and fork's signals are amplified at room temperature by a 79 dB amplifier and an I/V converter respectively. A more detailed diagram of the NEMS circuit can be found in b): "NA" refers to the network analyser input port; Z_{in} is the input impedance of this port, and Z_{out} is the output impedance of the signal generator driving the NEMS.

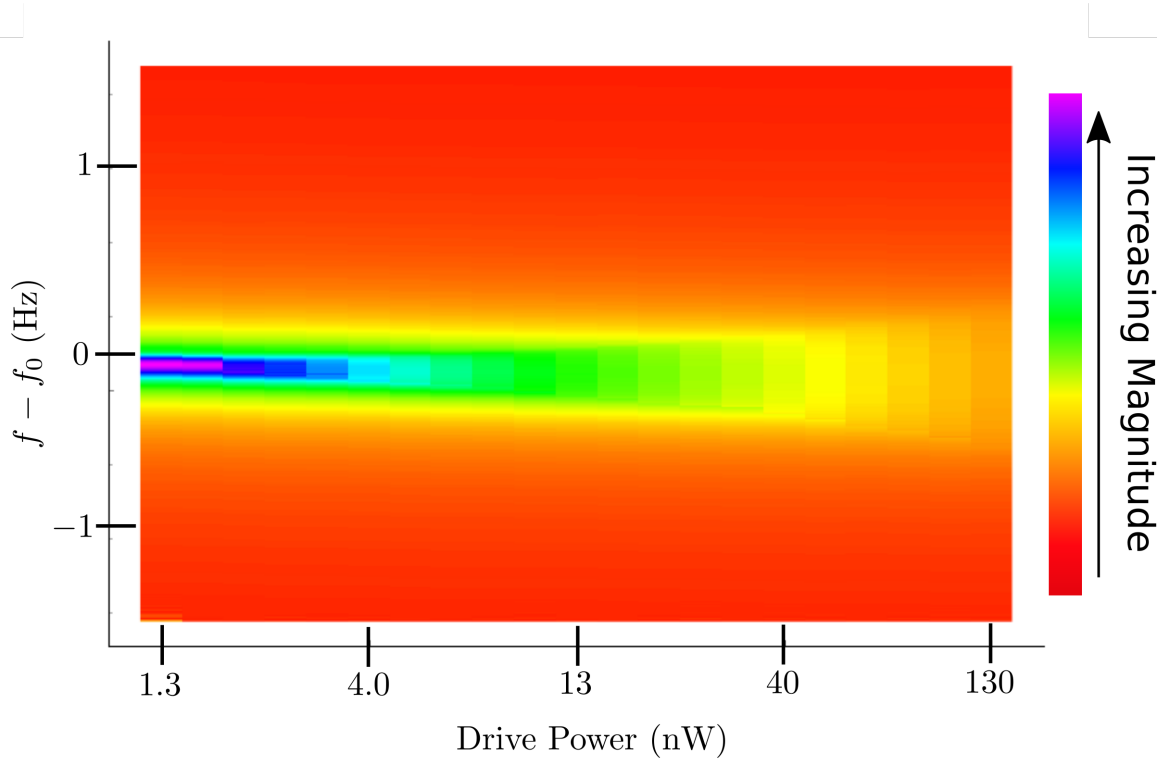

Figure 2.2: Response of the tuning fork as a function of frequency and drive power. Resonant frequency f_0 is 32 058 Hz. A cooler colour indicates a higher magnitude response. The plateauing of the response at high drive powers can be seen by the progressive broadening of the resonance peak.

where d_{11} is the longitudinal piezoelectric modulus of quartz; E is Young's modulus; and w, l, and h are the width, length, and height of the prongs, respectively[71]. In practice the fork constant is measured experimentally to be $2.5 \times 10^{-5}\,\mathrm{kg\,s^{-1}}$. Crucially, the drive force is independent of applied magnetic field, so the operation of the tuning fork is not affected by the magnetomotive scheme used to actuate the nearby beam-type resonator.

In order to produce vortices, the prongs of the fork must exceed a threshold velocity[26]. Velocity is modulated via drive force, which is in turn modulated via applied current. The power supplied to the fork is IV, where I is the current through the device, and the power dissipated by the fork is approximately Fv, where v is the velocity of the tips of the prongs. The velocity of the prongs is therefore

$$Fv = IV \quad \Rightarrow \quad v = 2I/a_f. \tag{2.3}$$

In practice the threshold velocity for turbulence generation is found by observing the current transmitted by the fork. Prior to the onset of turbulence the transmission of the fork as a function of drive frequency is Lorentzian. Once vortex generation begins, a characteristic "plateau" emerges, as seen in Fig. 2.2. Operating the device at a frequency within this plateau will generate quantum vortices. The operating point of the tuning fork during all our experiments is a frequency of 32 058 Hz and a drive power of 0.13 µW.

2.2 Doubly-clamped beam theory and operation

The aluminium-silicon nitride doubly-clamped beam-type resonator, hereafter referred to as the "NEMS", is positioned approximately 2 mm from the fork, as seen in Fig. 2.1, and is used to trap and probe vortices generated by the fork. The NEMS consists of an oscillating beam composed of a 30 nm thick aluminium layer used to actuate the device through a magnetomotive scheme atop a 100 nm thick Si_3N_4 layer which is responsible for most of the beam's mechanical properties. The beam is clamped on each end by thicker aluminium electrodes.

2.2.1 Physical parameters

A cross-section of the resonator beam can be seen in Fig. 2.3. The beam is a sister sample to that used in a previous study by Guthrie *et al.*[72], during which there was no significant observed longitudinal or torsional motion. Assuming pure flexural motion, then, the resonant frequency f_0 of a doubly-clamped beam with a rectangular cross

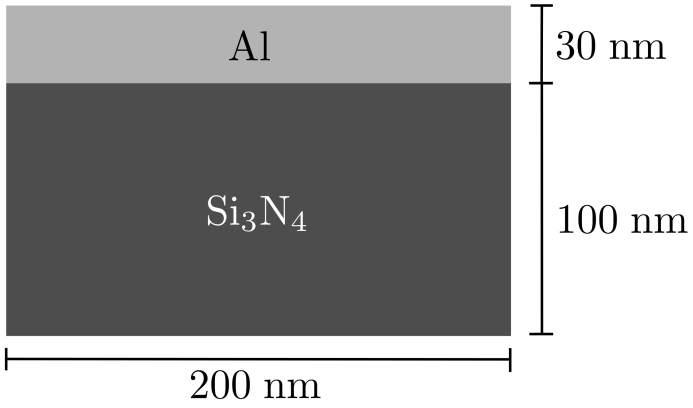

Figure 2.3: Cross section of the resonator beam.

section can be approximated as[73]

$$f_0 = \frac{k^2}{\pi\sqrt{48}}\frac{w}{l^2}\sqrt{\frac{E}{\rho_{beam}}}\sqrt{1+\gamma\left(\frac{w}{l}\right)^2\frac{T_0}{whE}} \tag{2.4}$$

where w is the width of the beam (200 nm), h the height of the beam (130 nm), l the length of the beam (70 µm), E Young's modulus (70 GPa), ρ_{beam} the mass density of the beam (averaged to 3062 $\mathrm{kgm^{-3}}$ accounting for both the silicon nitride and aluminium layers[72]), T_0 the intrinsic strain, and k and γ dimensionless constants that vary depending upon the harmonic (4.73 and 0.295 respectively for the fundamental mode). Resonant frequency in a vacuum at approximately 16 mK was measured to be 2.249 58 MHz, implying an intrinsic strain $T_0 = 3.66$ µN.

When immersed in helium, the added inertia of the fluid that must be displaced as the beam oscillates manifests as an increase in the effective mass m_{eff} of the device and a corresponding decrease in the resonant frequency. The ratio between the vacuum resonant frequency f_0^{vac} and the immersed resonant frequency f_0^{imm} is equal to[74]

$$\left(\frac{f_0^{vac}}{f_0^{imm}}\right)^2 = \frac{m_{eff}}{m_{bare}} = 1 + \beta\frac{\rho_{^4\mathrm{He}}}{\rho_{beam}} + B\frac{\rho_n}{\rho_{beam}}\frac{S}{V}\sqrt{\frac{\nu}{\pi\rho_n f_0^{imm}}} \tag{2.5}$$

Where m_{bare} is the mass of the beam in vacuum, $\rho_{^4\mathrm{He}}$ is the mass density of He-II (approximately 145 $\mathrm{kgm^{-3}}$ at 10 mK[75]), ρ_n is the mass density of the normal fluid fraction, S is the surface area of the beam, V is the volume of the beam, ν is the viscosity of the normal component, and β and B are dimensionless parameters dependent upon the geometry of the beam. For an infinitely long beam with a

rectangular cross section, $\beta = (\pi h)/(4w)$ and $B = 1$. At 10 mK, we consider the normal fluid fraction sufficiently small so as to render the term in Eq. (2.5) proportional to B negligible. Thus,

$$f_0^{imm} = \frac{f_0^{vac}}{\sqrt{1 + \beta \frac{\rho_{^4\mathrm{He}}}{\rho_{beam}}}} \approx 2.22285 \text{ MHz} \tag{2.6}$$

The observed f_0^{imm} is approximately 2.199 60 MHz. The discrepancy is likely due to the constant β imperfectly capturing the geometry of our device, which deviates from a perfectly straight, rectangular cross-section due to fabrication artefacts. Using $f_0^{imm} = 2.199\,60$ MHz, the actual value of β is 0.97.

2.2.2 Drive force

An AC current is applied to the beam in the presence of an external magnetic field directed straight up, perpendicular to both the beam and the substrate. The resultant Lorentz force $\mathbf{F} = \mathbf{I} \times \mathbf{B}$ drives the resonator, with drive frequency equal to the frequency of the drive current.

In practice, drive force is modulated by altering the power applied to the NEMS, rather than the current directly. If P_{in} is the power applied to the device after accounting for line attenuation, the drive force F_{Drive} is given by

$$F_{\mathrm{Drive}} = Bl\sqrt{\frac{P_{\mathrm{in}}}{Z_0}}, \tag{2.7}$$

where l is the length of the NEMS, approximately 70 µm, and Z_0 is the output impedance of the signal generator, approximately 100 Ω.

2.2.3 Beam velocity

The transmission of the NEMS is used to determine the motion of the beam. The oscillating beam is a current-carrying wire moving in a magnetic field, and therefore a back-emf is generated equal to

$$V_{emf} = \frac{d}{dt}(AB), \tag{2.8}$$

where A is the area across which the beam sweeps during one period, approximated as lx where l is the length and x the displacement of the centre of the beam, and B is the applied magnetic field. The maximum velocity of the centre of the resonating beam is related to the back-emf as

$$V_{emf} = lvB \quad \Rightarrow \quad v = \frac{V_{emf}}{lB}. \tag{2.9}$$

This emf manifests as an additional drop in voltage across the device when it is driven at resonance, compared to when the drive is far from resonance and displacement is negligible. Thus, the peak velocity of the beam can be determined by measuring the voltage drop when it is driven at resonance, after accounting for impedance from other sources. In practice, the maximum beam velocity is computed from the power dissipated by the NEMS at resonance. If $\Delta P_{\max}$ is the difference in power transmitted by the NEMS when driven far from resonance versus at resonance, then maximum beam velocity is

$$v_{\text{Beam}} = \frac{\sqrt{Z_i \Delta P_{\max}}}{Bl}, \tag{2.10}$$

where Z_i is the input impedance of the network analyser used to measure the transmitted signal, approximately $100\,\Omega$.

In both the linear and nonlinear regimes, the relationship between drive force and beam velocity is expected to take the form

$$v = bF^n, \tag{2.11}$$

where b and n are nonzero real numbers. In the linear regime, $n = 1$ as the Lortentz force gives

$$F_{mag} = IlB = \frac{vB^2l^2}{Z_0}. \tag{2.12}$$

When submerged, however, a NEMS oscillating with sufficient speed is expected to generate turbulence. Vortices serve to dissipate energy that would otherwise contribute to the motion of the resonator. Thus, in the nonlinear, turbulent regime, it is predicted that $n < 1$. In the case where turbulence generation is the primary loss mechanism, vortex nucleation may be modelled as a drag force on the oscillator beam. The drag equation gives $v \propto F^{0.5}$, so a value of $n = 0.5$ is expected in the nonlinear regime[53].

2.2.4 Beam losses

The relationship between the losses of the NEMS, defined as the inverse quality factor Q^{-1}, and the square of the external magnetic field B^2 is also used to characterise the behaviour of the NEMS. A qualitative plot of the expected relationship between these quantities for a vortex-free resonator can be seen in Fig. 2.4. At sufficiently high magnetic fields, magnetomotive damping is the primary dissipation mechanism and a linear relationship between Q^{-1} and B^2 is expected. If the impedance of the circuit is Z_0, the back-emf generated by the oscillating beam produces a back-current $I_{\text{mag}} = vBl/Z_0$. In accordance with Lenz's law, the current generates a force that

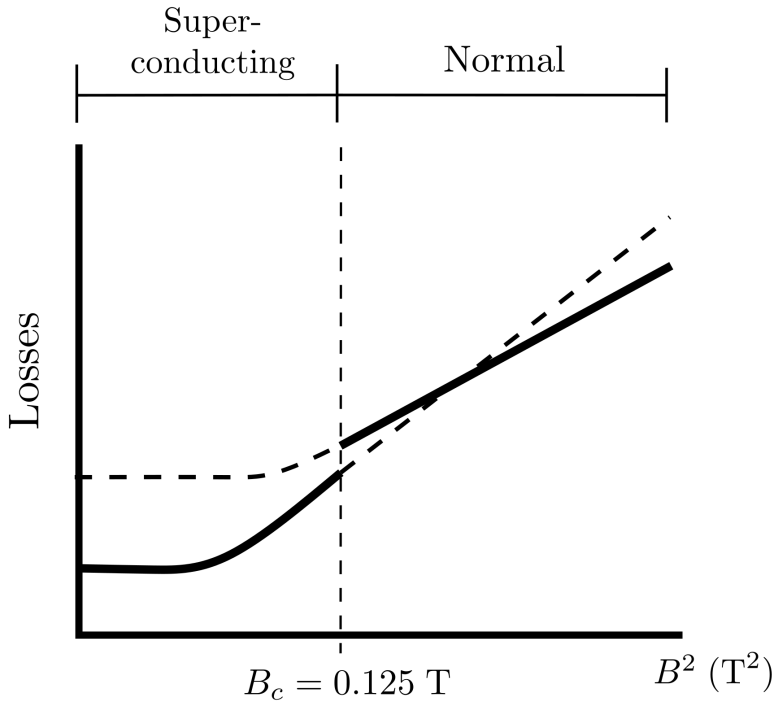

Figure 2.4: Qualitative plot of the expected dependence of losses on the square of the applied field for a vortex-free resonator. The superconducting transition field of 0.125 T is marked as a vertical dashed line. Solid lines indicate the actual expected response. Note the difference in slope between the superconducting and normal regimes; this is due to the inverse dependence of slope on the impedance of the circuit seen in Eq. (2.16).

opposes the drive force. The opposing force will have the same form as Eq. (2.12), but with the current being the back-current.

The quality factor for a mechanical resonator can be defined as

$$Q = 2\pi \frac{E_{\max}}{(\Delta E)_{\text{one period}}}, \tag{2.13}$$

where $E_{\max}$ is the maximum energy stored by the resonator and $(\Delta E)_{\text{one period}}$ is the energy dissipated by the resonator in one period of oscillation. The influence of dissipative mechanisms on the quality factor of a resonator can be represented as a sum of inverse quality factors

$$Q_{\text{tot}}^{-1} = \sum_i Q_i^{-1}, \tag{2.14}$$

where each Q_i is the ratio of the energy stored in the resonator and the power dissipated by a particular mechanism[76]. Assuming for simplicity that all energy is stored as kinetic energy, this gives for magnetomotive damping

$$Q_{\text{mag}} = 2\pi \frac{\frac{1}{2}mv^2}{Fv} = \frac{\pi f_0 m v^2}{\left(\frac{v^2 B^2 l^2}{Z_0}\right)} = \frac{\pi f_0 m Z_0}{B^2 l^2}. \tag{2.15}$$

Inverting this gives

$$Q_{\text{mag}}^{-1} = \frac{B^2 l^2}{\pi m Z_0}. \tag{2.16}$$

Thus, inverse quality factor will be proportional to the square of the magnetic field. At very low magnetic fields, other dissipation mechanisms such as clamping losses and inter-crystallite friction dominate and this linear relationship breaks down as seen in Fig. 2.4. Our measurements are performed in the linear regime, however, in which magnetomotive damping is expected to dominate.

An additional notable feature of Fig. 2.4 is a discontinuity at a critical field strength $B_c = 0.125\,\text{T}$. At fields lower than B_c, the thin aluminium beam of the NEMS becomes superconducting, resulting in a sudden increase in quality factor. An additional, less dramatic transition occurs at approximately 0.065 T, at which point the thick aluminium clamps of the resonator also become superconductors. However, this second transition was not observed to have a significant effect on the quality factor.

2.3 Trapped vortex states

When a vortex collides with the NEMS, it will create one of three possible states, illustrated in Fig. 2.5. The first and most common is a “no-vortex” state, denoted

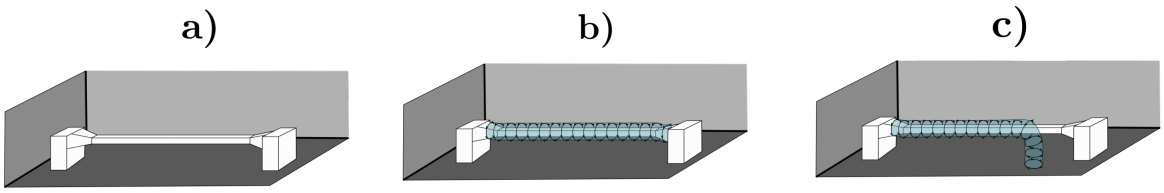

Figure 2.5: Qualitative depiction of various vortex states: a) the no-vortex state He_{nv}, b) the fully-trapped state $He_{||}$, and c) a partially-trapped state $He_{\perp}$. Note that the gradual curve off the beam in the $He_{\perp}$ image is an artistic generalisation. No experimental study of the geometry at such a pining point has been performed, though a theoretical analysis by Griffiths[3] suggests the vortex line forms a sharper cusp.

He_{nv} and illustrated in Fig. 2.5a. This is a vortex-free resonator that is additionally "topologically clean", with any vortices that may have previously been pinned to the device destroyed by the vortex collision. The vortex that collides with the NEMS is also either destroyed in this process or detaches and diffuses away. The second possible state is a "fully-trapped" state, denoted $He_{||}$ and illustrated in Fig. 2.5b. This state is created when the colliding vortex ring splits and each end of the vortex becomes pinned to each end of the NEMS beam, so that the entire length of the beam is enveloped by circulating superfluid.

The third possible state is a "partially-trapped" state, denoted $He_{\perp}$ and illustrated in Fig. 2.5c. Rather than both ends of the vortex becoming pinned to the ends of the beam as in a $He_{||}$ state, in a $He_{\perp}$ state at least one end instead becomes pinned to another structure in the sample cell. Only part of the beam is enveloped in circulating superfluid, and there is a length of vortex not aligned with the beam. Typically, an end of the vortex not pinned to the resonator becomes pinned to the substrate directly below the beam, a distance of approximately 1 µm. This is due to energy conservation. Vortices carry an energy per unit length, so it is energetically favourable for a vortex to have minimal length. The shortest path from the NEMS beam to another structure the vortex can be pinned to is in almost all cases straight down, from the beam to the substrate. It is thus expected that almost all partially-trapped states will be pinned in the manner seen in Fig. 2.5c, although the length of beam enveloped by circulation is different in every partially-trapped state.

The creation of neither partially- nor fully-trapped states has been observed without the action of the tuning fork. While theoretically possible due to, for example, a thermally-generated vortex impinging on the device during cool-down of the system, this appears to be rare as it has not yet been observed and, regardless, is very unlikely to occur when the system is operating in its steady state at temperature.

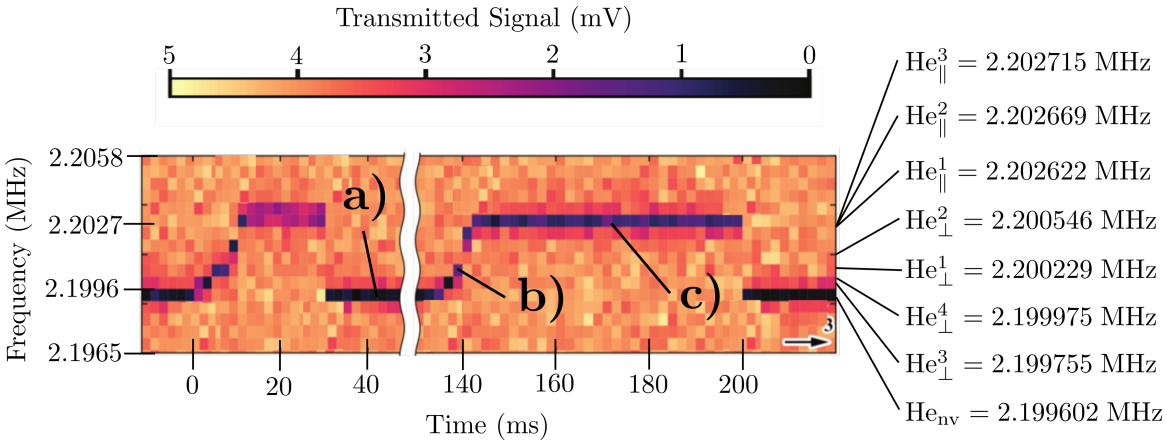

Figure 2.6: Response of the NEMS during two trapping events. The y-axis is drive frequency, and a cooler colour indicates a greater magnitude response. The NEMS is in a He_{nv} state at (a), a $He_{\perp}$ state at (b), and a $He_{||}$ state at (c). The names and resonant frequencies of all vortex states referred to in this study can be seen to the right of the histogram.

A fourth state, the "vacuum" state, denoted He_{vac}, corresponds to the NEMS in vacuum. It is used as a reference point to determine which behaviours are due to interaction with the superfluid and which are due to the intrinsic properties of the NEMS. Measurements of the He_{vac} state are performed at approximately 16 mK, as this is the lowest achievable temperature in the sample cell without the presence of helium.

When a vortex becomes trapped, it has a profound effect on some behaviours of the resonator. One of the most dramatic changes is in resonant frequency. When a vortex becomes fully trapped, the tension of the beam increases due to the force of interaction between the trapped vortex a distance d above the substrate and its image a distance d beneath the substrate. The force per unit length $\mathbf{f}$ due to this interaction is given by[72]

$$\mathbf{f} = \boldsymbol{\kappa} \times \mathbf{j} \tag{2.17}$$

where $\boldsymbol{\kappa}$ is the circulation quantum in the direction of vorticity (parallel to the beam) and $\mathbf{j} = \rho_{^4\mathrm{He}}\mathbf{v}_{imag}$ is the flow density due to the image vortex, which at the location of the beam generates a fluid velocity

$$\mathbf{v}_{imag} = \frac{\kappa}{2\pi(2d)}\hat{\phi} \tag{2.18}$$

with the $\hat{z}$ direction taken to be parallel with the vorticity. The magnitude of the

force per unit length on the beam is then

$$f = \frac{\kappa^2 \rho_{^4\mathrm{He}}}{4\pi d} \tag{2.19}$$

The additional tension T_{vort} due to this force per unit length is[72]

$$T_{vort} = \frac{1}{2} f \frac{l^2}{h} \tag{2.20}$$

Based on the experimental parameters of our system ($l = 70\,\mu\mathrm{m}$, $h = 130\,\mu\mathrm{m}$, $d = 1\,\mu\mathrm{m}$), this would suggest $T_{vort} = 2\,\mathrm{nN}$. Adding this to the equilibrium tension T_0 in Eq. (2.4) and accounting for the increased effective mass due to immersion using Eq. (2.6), the resonant frequency in a fully-trapped state is predicted to be 2.200 20 MHz, an increase of 600 Hz.

Experimental observation of fully-trapped states indicates the resonant frequency upshifts by approximately 3.1 kHz relative to the $\mathrm{He_{nv}}$ resonance, within an order of magnitude of the theoretical estimate. When a vortex becomes partially-trapped, the resonant frequency again upshifts, but by less than 3.1 kHz. The degree of deviation from the $\mathrm{He_{nv}}$ resonance is believed to depend upon the length of beam that is enveloped by circulation, with greater deviation occurring when more of the beam is enveloped. States are distinguished experimentally based on the shift in resonant frequency. This effect is illustrated in Fig. 2.6, which depicts the transmission of the resonator as a function of drive frequency during two separate trapping events. In these events, the vortex initially becomes partially-trapped, before gradually shifting into a fully-trapped configuration. This is typical of the onset of a fully-trapped state, though most partially-trapped states do not evolve into fully-trapped states.

Chapter 3

Resonator Response Analysis

Three fully-trapped states and four partially-trapped states, along with the no-vortex and vacuum states, were created and measured. Not all measurements were performed on every state. These states will be denoted as shown in Table 3.1 and Fig. 2.6.

3.1 Losses and magnetic field

The dependence of the losses experience by the NEMS, equal to the dimensionless linear drag coefficient $\widetilde{\zeta}$ or the inverse quality factor Q^{-1}, on applied magnetic field B was measured for the beam in the $\mathrm{He}_{\mathrm{vac}}$, $\mathrm{He}_{\mathrm{nv}}$, $\mathrm{He}^1_{\parallel}$, $\mathrm{He}^2_{\parallel}$, $\mathrm{He}^3_{\parallel}$, $\mathrm{He}^2_{\perp}$, $\mathrm{He}^3_{\perp}$, and $\mathrm{He}^4_{\perp}$ states.

Quality factor at each magnetic field was found by fixing drive power and sweeping drive frequency about resonance. The magnitude of the transmission coefficient S_{21} is measured at each frequency. If the FWHM of the resonance peak formed by the distribution of S_{21} is Δf and the resonant frequency is f_0, Q is

$$Q = \frac{f_0}{\Delta f}. \tag{3.1}$$

In some cases, sweeps were done at multiple drive powers; where this is the case, the results presented here are an average of all sweeps done for a given state. A comparison of states $\mathrm{He}_{\mathrm{vac}}$, $\mathrm{He}_{\mathrm{nv}}$, $\mathrm{He}^1_{\parallel}$, $\mathrm{He}^2_{\parallel}$, and $\mathrm{He}^3_{\parallel}$ can be seen in Fig. 3.1. A comparison of states $\mathrm{He}^2_{\perp}$, $\mathrm{He}^3_{\perp}$, and $\mathrm{He}^4_{\perp}$ can be seen in Fig. 3.2. A comparison of states $\mathrm{He}_{\mathrm{vac}}$, $\mathrm{He}_{\mathrm{nv}}$, $\mathrm{He}^2_{\parallel}$, and $\mathrm{He}^2_{\perp}$ can be seen in Fig. 3.3. In all cases, fits are of the form $Q^{-1} = m(B^2) + b$, with m and b free parameters. The value of the fit parameters are given in Table 3.2.

As seen in Fig. 3.1, the $\mathrm{He}_{\mathrm{vac}}$, $\mathrm{He}_{\mathrm{nv}}$, and all three $\mathrm{He}_{\parallel}$ states behave very similarly, and very linearly. The $\mathrm{He}_{\mathrm{vac}}$ state exhibits slightly lower losses, a difference of $Q^{-1}_{\mathrm{ac}} = 1.8 \times 10^{-6}$ relative to the $\mathrm{He}_{\mathrm{nv}}$ state. This is expected as acoustical loss via phonon emission is a dissipation mechanism available to immersed states but not possible in

State Label	Resonant Frequency (Hz)
He_{vac}	2250109
He_{nv}	2199602
$He^1_{\parallel}$	2202622
$He^2_{\parallel}$	2202669
$He^3_{\parallel}$	2202715
$He^1_{\perp}$	2200229
$He^2_{\perp}$	2200546
$He^3_{\perp}$	2199755
$He^4_{\perp}$	2199975

Table 3.1: State labels and resonant frequencies. Resonant frequency is estimated from a Lorentzian fit (Eq. (1.33)) of the data when drive force is tuned so there is no noticeable nonlinearity.

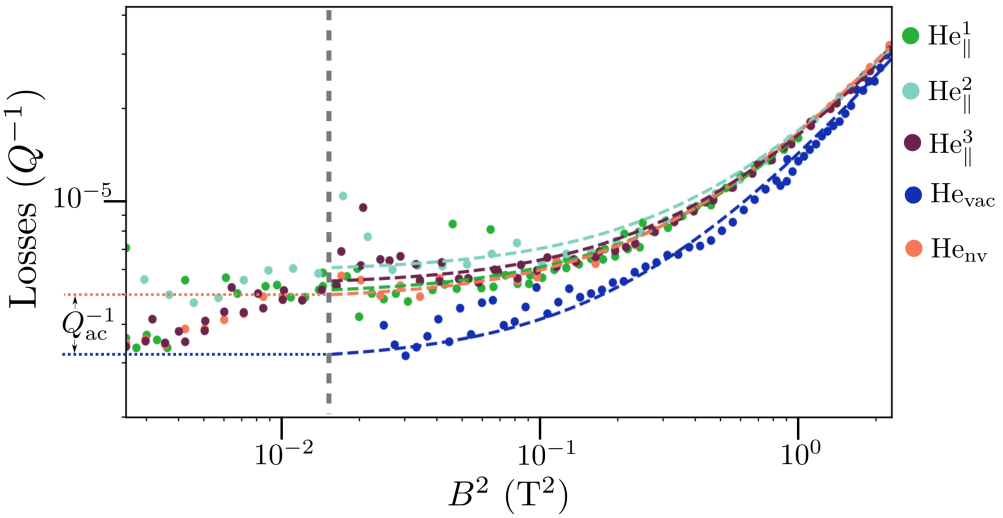

Figure 3.1: Plot of losses vs B^2 measurements for various fully-trapped and vortex-free states. Dashed lines are linear regression fits. A vertical dashed line marks the superconducting transition field 0.125 T. Fit parameters can be found in Table 3.2. The fully-trapped and no-vortex states demonstrate very similar losses. The difference in losses $Q^{-1}_{ac} = 1.8 \times 10^{-6}$ between states He_{nv} and He_{vac} is attributed to acoustical losses not present in a vacuum.

a vacuum. There is no significant difference between the response of the $He_{\parallel}$ and He_{nv} states, indicating that the existence of a fully-trapped vortex has little effect on the dissipation mechanisms available to the resonator. The strong linear relationship between Q^{-1} and B^2 for the He_{vac}, He_{nv}, and $He_{\parallel}$ states above the superconducting transition field 125 mT agrees with theoretical predictions described in Section 2.2. This suggests that in these states there is minimal interaction with the superfluid at the drive powers accessed during these measurements, with the exception of some energy loss via phonon emission when the NEMS is immersed.

State	m	b
He_{vac}	1.1×10^{-5}	3.0×10^{-6}
He_{nv}	1.2×10^{-5}	4.8×10^{-6}
$He_{\parallel}^{1}$	1.1×10^{-5}	5.0×10^{-6}
$He_{\parallel}^{2}$	1.1×10^{-5}	5.9×10^{-6}
$He_{\parallel}^{3}$	1.1×10^{-5}	5.3×10^{-6}
$He_{\perp}^{2}$	1.2×10^{-5}	2.1×10^{-5}
$He_{\perp}^{3}$	1.4×10^{-5}	1.2×10^{-5}
$He_{\perp}^{4}$	2.5×10^{-5}	2.9×10^{-5}

Table 3.2: Fit parameters for regression lines in Fig. 3.3, Fig. 3.2, and Fig. 3.1. Lines are of the form $Q^{-1} = mB^2 + b$.

The partially-trapped states exhibit losses which vary depending upon state, as seen in Fig. 3.2. The qualitative behaviour of the three states is very similar, although there is a significant quantitative difference in the losses experienced by each. This quantitative difference does not appear to correlate with resonant frequency. As resonant frequency is believed to be closely related to the length of resonator beam enveloped by circulation, this suggests that the additional dissipation in a partially-trapped state is not governed by the portion of vortex aligned with the beam. Rather, it is believed to be produced by the motion of the unaligned filament(s), with some possible dependence upon their length and location.

In all partially-trapped states losses are significantly higher than in the He_{vac}, He_{nv}, and $He_{\parallel}$ states, as illustrated in Fig. 3.3. This indicates the existence of a dissipation mechanism in partially-trapped states not seen in any other state. We hypothesise that this dissipation comes from phonons radiated by the unaligned portion of the partially-trapped vortex. The motion of the resonator beam will couple with the unaligned filament, likely inducing Kelvin waves. These Kelvin waves would then cascade as described in Section 1.2.2, ultimately leading to a gradual emission of energy via phonons and, possibly, self-reconnections. Both these processes result in an additional loss of energy, which would manifest as greater dissipation. The latter process is suspected due to previous experimental observations of a vibrating wire in

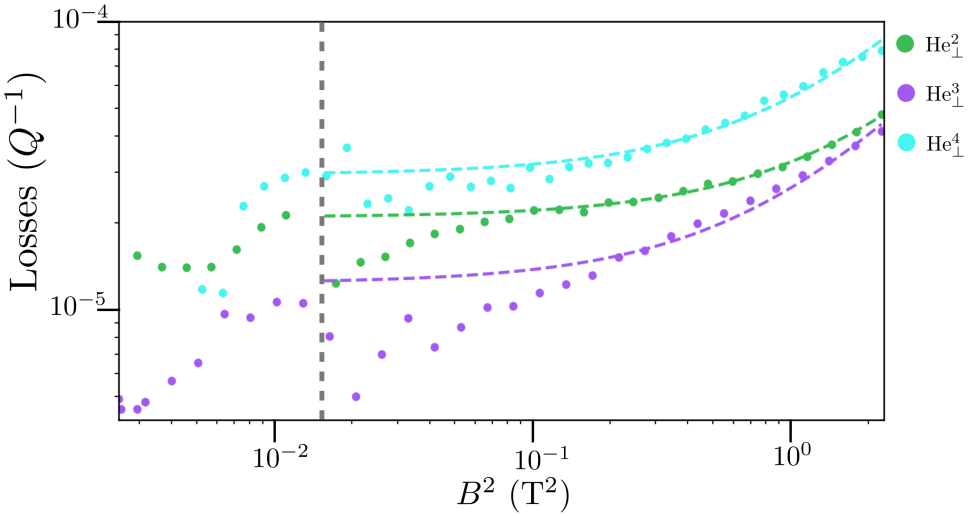

Figure 3.2: Plot of losses vs B^2 measurements for various partially-trapped states. Dashed lines are linear regression fits. A vertical dashed line marks the superconducting transition field 0.125 T. Fit parameters can be found in Table 3.2. The qualitative behaviour of the three states is very similar. The quantitative difference does not correlate with resonant frequency, and is therefore attributed to differences in the unaligned filaments of each state.

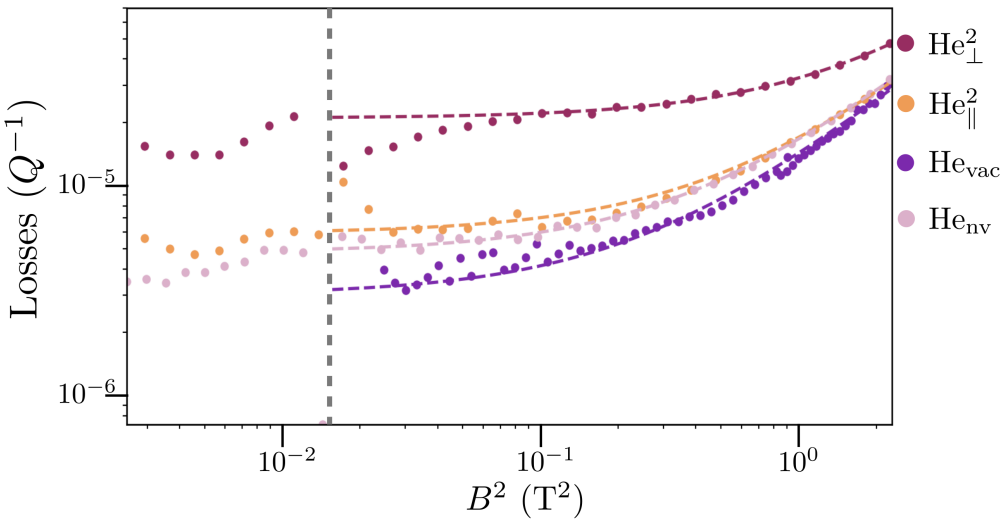

Figure 3.3: Plot of losses vs B^2 for various vortex states. Dashed lines are linear regression fits. A vertical dashed line marks the superconducting transition field 0.125 T. Fit parameters can be found in Table 3.2. The partially-trapped state exhibits significantly greater losses than other states, suggesting the presence of an unaligned vortex filament provides an additional dissipation mechanism.

superfluid ^{3}He. In these studies, Bradley *et al.* found a periodic fluctuation in wire velocity between two critical values during the onset of turbulence generation, which they attribute to the periodic emission of vortices created by self-reconnections on the perturbed trapped vortex line[34,77]. Hashimoto *et al.* found that a wire vibrating at velocities too low to nucleate turbulence in superfluid ^{4}He generates quantum vortices when a vortex becomes pinned between the wire and the wall of the sample cell, which they likewise attribute to vortex rings generated by high-amplitude Kelvin waves[78,79].

The difference in losses between different partially-trapped states could be related to the position and number of unaligned filaments. A partially-trapped vortex with two unaligned filaments would be expected to have higher losses than a similar vortex with one end pinned to a resonator clamp. The beam exhibits nonuniform deflection, with higher-amplitude motion near the centre of the beam and relatively little displacement near the clamps. Therefore, an unaligned filament extending from the middle of the beam would be more violently excited than a filament extending from one of the ends, and would dissipate more energy.

If the above picture is accurate, we would expect to see evidence of increased drag in partially-trapped states, beyond that seen in vortex-free or fully-trapped states. Our study of beam velocity as a function of applied drive force provides such evidence.

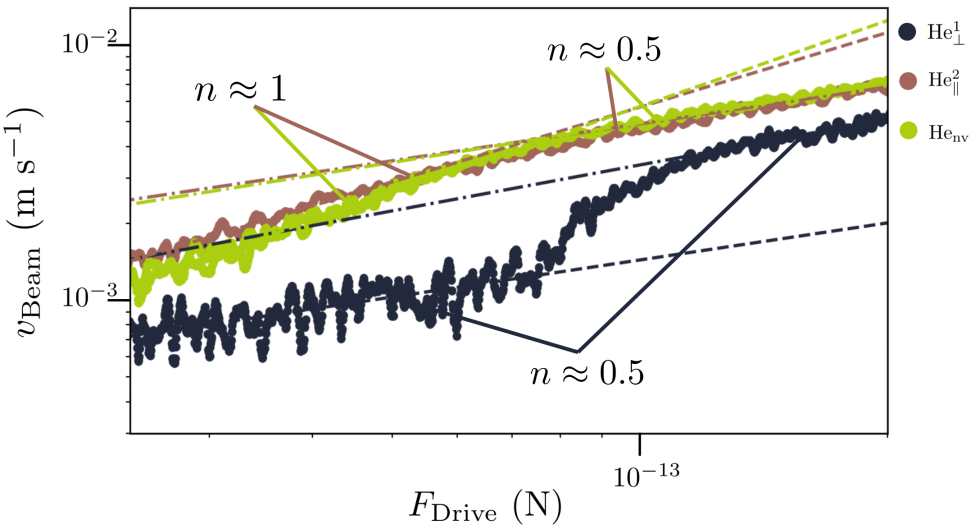

Figure 3.4: Plot of velocity-force measurements for states He_{nv}, $\text{He}_\parallel^2$, and $\text{He}_\perp^1$ at 0.3 T. Data has been smoothed with a Savitzky–Golay filter. Unlike in the fully-trapped and no-vortex states, the partially-trapped state has no linear regime in which velocity is directly proportional to drive force, suggesting the unaligned filament provides an additional means of generating turbulence even at low drive forces.

3.2 Beam velocity and drive force

State	b Pre-v_c	n Pre-v_c	b Post-v_c	n Post-v_c
$\text{He}_\parallel^2$	2.5×10^{10}	0.97	8.8×10^3	0.48
He_{nv}	2.1×10^{12}	1.12	2.5×10^4	0.52
$\text{He}_\perp^1$	2.7×10^3	0.48	2.0×10^5	0.60

Table 3.3: Fit parameters for regression lines in Fig. 3.4. Lines are of the form $v = bF^n$, and v_c refers to the critical velocity.

The dependence of NEMS beam velocity v on applied drive force F was measured for states He_{nv}, $\text{He}_\parallel^2$, and $\text{He}_\perp^1$. Magnetic field was held fixed at 0.3 T and the NEMS was driven at its resonant frequency as drive power was swept from 0.1 fW to 100 fW. Drive power is directly related to drive force as described in Section 2.2. Results can be seen in Fig. 3.4. Fit parameters can be found in Table 3.3; fits are of the form $v = bF^n$, with b and n free parameters.

The fully-trapped and no-vortex states exhibit highly consistent behaviour, having largely coinciding linear regimes in which $n \approx 1$ and nonlinear regimes in

which $n \approx 0.5$. The transition to turbulent behaviour is not as abrupt as expected, with no single critical velocity distinguishable. Rather, a small range of velocities appears to form a "critical regime", over which the onset of turbulence is gradual.

Partially-trapped states deviate significantly from other states. A "kink" can be seen in the response in Fig. 3.4, indicating the existence of a critical velocity believed to be the onset of turbulence nucleation by the beam. However, even at velocities below the kink, $n \approx 0.5$ in state $\mathrm{He}^1_\perp$, and in all other partially-trapped states observed. Significant drag even below the critical velocity is thus inferred, via a mechanism not present in any other state. As the primary feature distinguishing partially-trapped states from fully-trapped states is the presence of unaligned vortex filaments, these filaments are believed to be the source of the additional turbulence. This would support the theory posed in Section 3.1, with energy loss via phonons radiated by Kelvin waves and possibly the emission of vortices due to self-reconnections manifesting as increased drag.

3.3 Spectrum analysis

A frequency domain analysis of the signal transmitted by the NEMS in states $\mathrm{He}_{\mathrm{nv}}$, $\mathrm{He}^3_\parallel$, $\mathrm{He}^3_\perp$, and $\mathrm{He}^4_\perp$ reveals the existence of phase modulation in partially-trapped sates. Magnetic field was fixed at 1 T and drive frequency was fixed at resonance. The frequency components of the transmitted signal were then parsed for various drive powers. The results can be seen in the histograms in Fig. 3.5 and Fig. 3.6.

In all four states, the most significant component is at the resonant frequency, as expected for a monochromatic drive signal at resonance. The $\mathrm{He}^3_\perp$ and $\mathrm{He}^4_\perp$ states, however, exhibit frequency sidebands, occurring at integer multiples of 9.8 Hz relative to the resonant frequency as noted in Fig. 3.5. The magnitude of each sideband does not increase monotonically with increasing drive power, as the resonance component does. Instead, sideband magnitude appears to oscillate about an increasing mean as drive power is increased. The magnitude of the sidebands generally decreases with distance from the resonant frequency, but at some drive powers more distant sidebands can have higher magnitude than those closer to resonance.

Sidebands are never observed in $\mathrm{He}_{\mathrm{nv}}$ or $\mathrm{He}_\parallel$ states, and are not present in the input signal. They are observed in most, though not all, $\mathrm{He}_\perp$ states, always in the configurations seen in Fig. 3.5 and Fig. 3.6: evenly spaced at integer multiples of 9.8 Hz relative to the state's resonant frequency, and with the same nonmonotonic dependence of magnitude on drive power.

Mathematically, this effect matches the response expected of a phase (or, alternatively, frequency) modulated device. Consider a phase modulated response

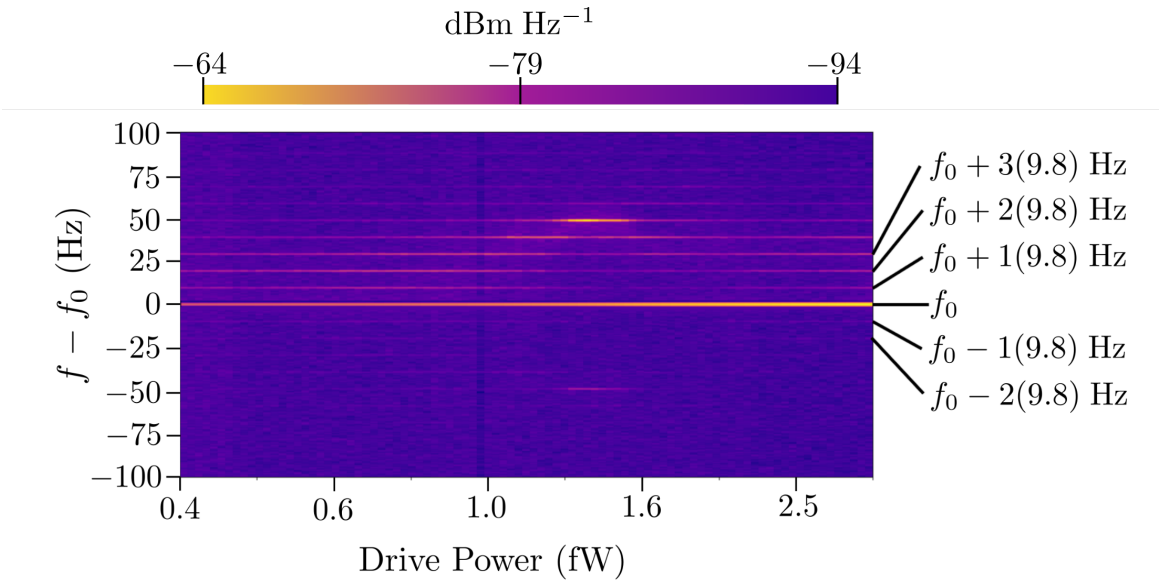

Figure 3.5: Histogram of NEMS spectral response as a function of drive power for state $He^3_\perp$. Response magnitude is represented by colour; warmer colour indicates higher magnitude. The resonant frequency $f_0 = 2.199\,755$ MHz and the $n = \pm 1,\ \pm 2,\ 3$ sidebands are labelled.

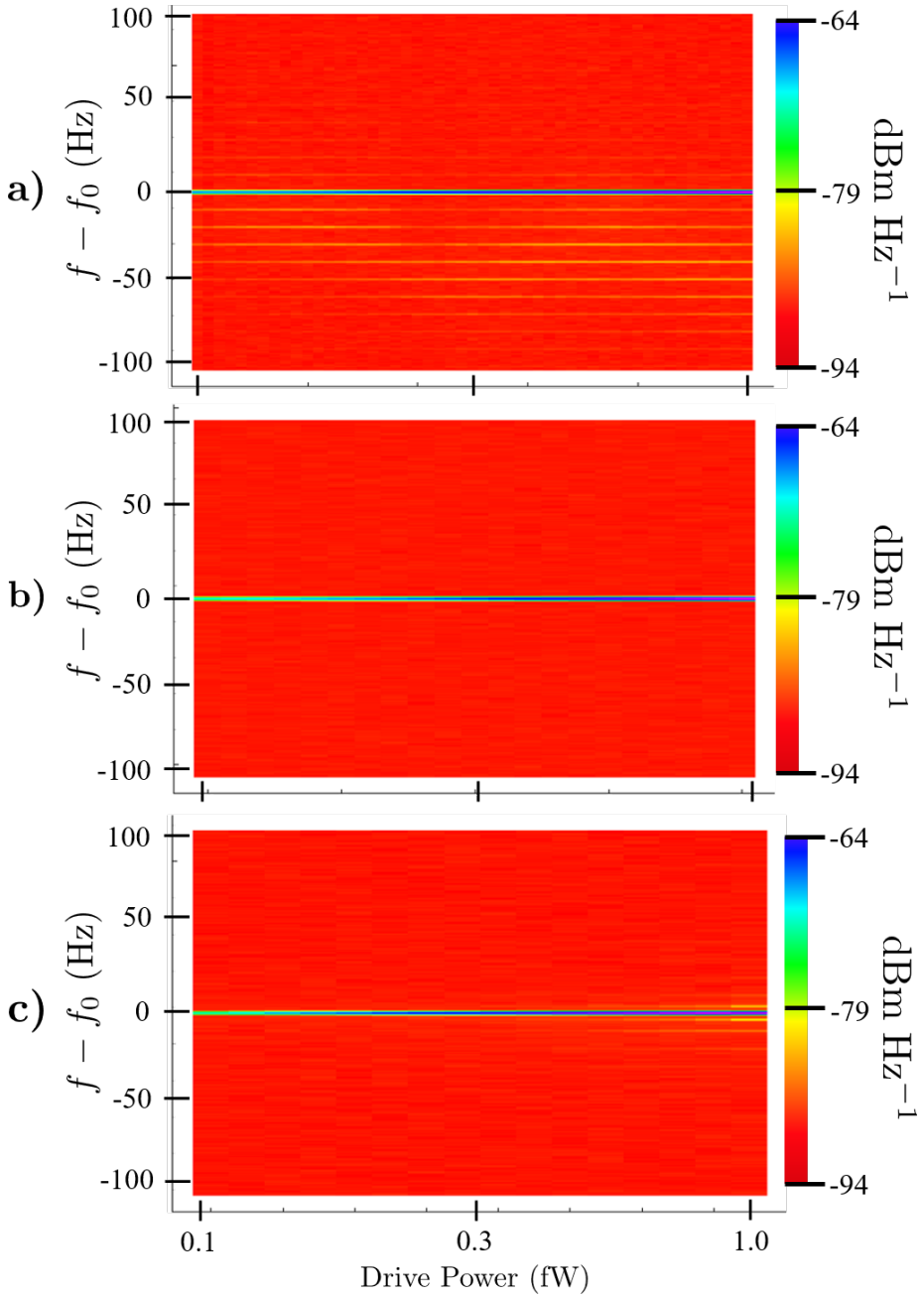

Figure 3.6: Histogram of NEMS spectral response as a function of drive power for states: a) $He^4_\perp$, b) He_{nv}, and c) $He^3_\parallel$. Response magnitude is represented by colour; cooler colour indicates higher magnitude. Colouring between different states is not to scale. Resonant frequency f_0 is 2.199 975 MHz for state $He^4_\perp$, 2.199 602 MHz for state He_{nv}, and 2.202 715 MHz for state $He^3_\parallel$.

at the resonant frequency ω_0

$$x(t) = A \exp\left(i\omega_0 t + b \sin(\Omega t)\right), \tag{3.2}$$

where A is the unmodulated amplitude, b is the modulation magnitude, and Ω the modulation frequency. A Jacobi-Anger expansion then returns

$$x(t) = Ae^{i\omega_0 t} \sum_{n=-\infty}^{n=\infty} J_n(b) e^{in\Omega t}, \tag{3.3}$$

where J_n is the n^{th} Bessel function of the first kind. The response has an infinite number of sidebands, each at a frequency of $\omega_0 \pm n\Omega$, $n \in \mathbb{Z}$. If $\Omega = 9.8\,\text{Hz}$, this matches the experimental observations. The magnitude of the n^{th} sideband will be $AJ_n(b)$. For integer values of n, $J_n(b)$ is oscillatory, with the magnitude of successive extrema decreasing with increasing b. If the parameter b increases monotonically with increasing drive power, this explains nonmonotonic behaviour of sideband magnitudes. The increasing mean can be explained by a dependence of the unmodulated amplitude A on drive power. Alternatively, this effect could be due to a second signal with much higher frequency, exactly 9.8 Hz greater or lower than the resonant frequency of the system. However, no hypothesis regarding the physical origin of such a signal could be found, especially given the fact that such a signal would have to change depending upon the vortex state to always be 9.8 Hz relative to resonance. A 9.8 Hz signal therefore appears more likely. AM modulation is likewise considered unlikely as multiple modulation signals would be required to achieve the observed sideband behaviour.

The source of this phase modulation is also currently unknown, however. Helmholtz resonance is a possible culprit. The sample cell and the attached pipe used to deliver helium to the cell form a system analogous to a Helmholtz resonator. The resonant frequency f_H of such a system will be approximately

$$f_H = \frac{v_c}{2\pi} \sqrt{\frac{A_n}{V_c L_{\text{eq}}}} \tag{3.4}$$

where v_c is the speed of sound, A_n is the cross-sectional area of the cavity neck, V_c is the volume of the cavity, and L_{eq} is the equivalent length of the neck accounting for end correction, equal to $L_n + 0.3d_n$ where L_n is the actual length of the neck and d_n the diameter of the neck. Assuming the pipe is a neck with cross-sectional area $0.64\,\text{mm}^2$, length 33 cm and diameter 0.9 mm, and the sample cell is a cavity with volume $2.6\,\text{cm}^3$, $f_H \approx 33$ Hz, within an order of magnitude of the observed modulation signal.

It is unclear why the excitation of a Helmholtz resonance would induce sidebands only in partially-trapped states, however, or why some partially-trapped states do not

exhibit modulation. Given that the distinguishing feature of partially-trapped states is the existance of an unaligned filament, it seems likely that the motion of the unaligned filament provides coupling between the source of the modulation frequency and the beam. Kelvin waves induced by oscillator motion are thought to be an unlikely source, as standing waves in the filament are predicted to have frequencies in the hundreds of kilohertz, far too high to account for a 9.8 Hz modulation signal.

Further work is needed to determine the origin of the modulation. One means of determining whether the modulation is related to Kelvin waves is by varying pressure in the sample cell. Core radius depends upon pressure, with one study finding a 30% increase as pressure was increased from 0 to 24 atm[19]. As demonstrated by Eq. (1.24), Kelvin wave frequency depends upon core radius. If the Kelvin waves are involved in generating the modulation signal, the spacing between sidebands should decrease with increasing pressure. To test for the influence of a Helmholtz resonance, the length of the pipe leading to the sample cell may be shortened or elongated. If a Helmholtz mechanism is contributing to the effect, sideband spacing should change.

Mechanical resonance of the sample cell was also considered as a possible source of the modulation signal. However, utilising the derivation of mechanical resonances in a hollow cylinder provided by Wang and Lai[80], the estimated fundamental frequencies of longitudinal, flexural, and torsional motion of the sample cell are 0.8 MHz, 0.2 MHz, and 0.8 MHz, respectively. Resonance of the sample cell is therefore not believed to be the source of the modulation signal. Vibrations from sources outside the sample cell are also considered unlikely. The cryostat is suspended by dampers to insulate it from the laboratory environment, and heavy machinery such as the pulse tube are kept in a separate room.

Attempts to directly excite the sidebands in the $He^3_\perp$ and $He^4_\perp$ states were unsuccessful. Amplitude modulation was induced on the input signal to attempt to drive the sideband resonances, as shown in Fig. 3.7a. If sideband modes were being excited, a much stronger response would be expected when the AM rate is equal to a sideband frequency. This does not appear to be the case. In addition to the $10 - 100$ Hz sweep in Fig. 3.7a, additional sweeps with AM rate as low as 0.1 Hz and as high as 10 kHz were performed, with no discernible impact on sideband magnitude.

Driving the system at sideband frequencies also had no effect on sideband magnitude. By applying a drive signal at a sideband frequency, it was hoped that the source of the modulation could be directly driven, which could back-couple with the NEMS and alter the magnitude of other frequency components. As shown in Fig. 3.7b and 3.7c, however, a drive signal at a sideband frequency has no greater effect on the magnitude of other frequency components than a drive signal at a frequency between sidebands.

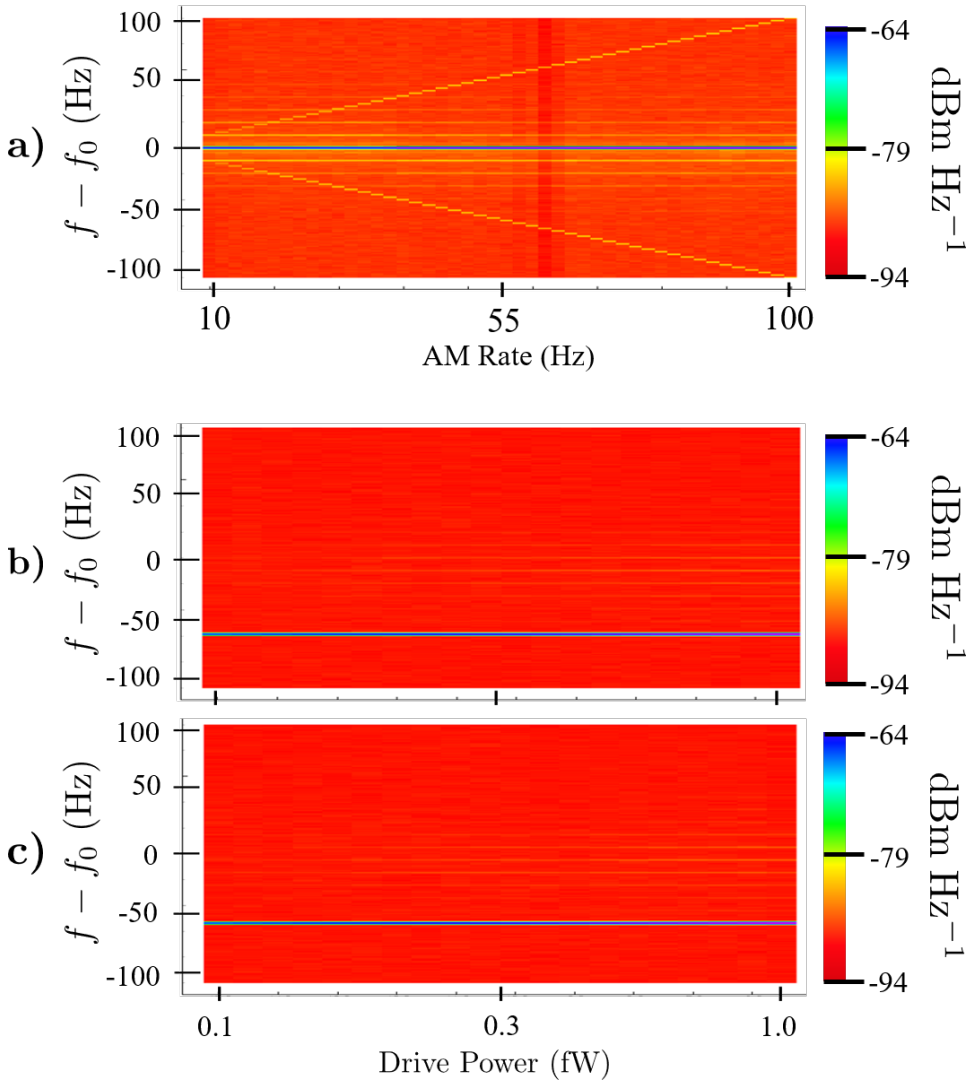

Figure 3.7: Histogram of NEMS spectral response for a) state $He^3_\perp$ with an AM input signal with 5% depth and increasing modulation rate, b) state $He^4_\perp$ with a non-modulated drive signal at the frequency of sideband $n = -6$, and c) state $He^4_\perp$ with a drive signal at a frequency between sidebands $n = -6$ and $n = -5$. Response magnitude is represented by colour; cooler colour indicates higher magnitude. Colouring between different states is not to scale. Resonant frequency f_0 is 2.199 755 MHz for state $He^3_\perp$ and 2.199 975 MHz for state $He^4_\perp$.

Chapter 4

Duffing Oscillator Fit

4.1 Duffing force in a partially-trapped state

Along with intrinsic nonlinearities, the influence of a partially-trapped vortex on the NEMS may be modelled as another Duffing-type force. Consider the situation depicted in Fig. 2.5c, with one end of the vortex pinned to the substrate a distance h directly below the beam. Let ε be the energy per unit length of the vortex and l be the length of the unaligned filament. The length of the filament is a function of displacement

$$l = \sqrt{x^2 + h^2} \tag{4.1}$$

The tension of the vortex line may be derived from its energy, giving

$$F_{\text{Vortex}} = \frac{d}{dx}(\varepsilon l) = \varepsilon x (x^2 + h^2)^{-1/2}. \tag{4.2}$$

Assuming displacement is small, a Taylor expansion of $(x^2+h^2)^{-1/2}$ about $x = 0$ then gives

$$F_{\text{Vortex}} \approx \varepsilon x \left(\frac{1}{h} - \frac{x^2}{2h^3} \right) = \frac{\varepsilon}{h} x - \frac{\epsilon}{2h^3} x^3. \tag{4.3}$$

The influence of the vortex may thus be modelled as two effects: a positive addition to the linear restoring force which will shift the resonant frequency, and a negative addition to the nonlinear restoring force which will soften the resonator. It is with this in mind that the Duffing model was used to fit the frequency response of the NEMS in fully-trapped, partially-trapped, and no-vortex states.

4.2 Data processing

The frequency response of the Duffing oscillator (Eq. (1.43)) takes drive frequency as the independent variable and oscillator amplitude as the dependent variable. The

amplitude of oscillation x_0 must therefore be extracted from the raw experimental data in order to fit Eq. (1.43) and estimate the Duffing parameter α.

The motion of the NEMS is encoded in its complex transmission. The device is actuated and probed using a network analyser (NA). The NA is a two-port device which emits a signal at Port 1 that passes through the NEMS, actuating it. The signal transmitted by the NEMS is then read at Port 2. For each drive frequency ω at which the NEMS response is sampled, the NA returns the complex transmittance S_{21}, defined as

$$S_{21} = \frac{V_2^{\text{out}}}{V_1^{\text{in}}}, \tag{4.4}$$

where V_1^{in} is the complex voltage applied at Port 1 and V_2^{out} the complex voltage received by Port 2. The modulus of the complex-valued transmission $|S_{21}|$ is typically used when computing displacement. A Lorentzian curve is fitted to the transmission coefficient $|S_{21}|(\omega)$ data, from which quality factor Q and background signal S_{bkg} are extracted. The power dissipated due to NEMS motion ΔP at a given drive frequency ω can then be computed via

$$\Delta P(\omega) = AP_{\text{in}}\{[S_{\text{bkg}}]^2 - [|S_{21}|(\omega)]^2\}, \tag{4.5}$$

where P_{in} is the power applied by the network analyser and A is a scale factor accounting for both the attenuation and gain of the transmission line and amplifier separating the NEMS output and the NA. This is the power dissipated by the NEMS alone, with other electrical losses factored out.

Amplitude of oscillation can then be found from the definition of the quality factor. Assuming energy is stored purely mechanically in one degree of freedom, the maximum stored energy E_{max} in Eq. (2.13) can be written

$$E_{\text{max}} = \frac{1}{2} m\omega_0^2 x_0^2, \tag{4.6}$$

where m is the effective mass of the beam. One period of oscillation is approximately $2\pi/\omega$ assuming drive frequency is close to the resonant frequency, so the energy dissipated over one period can be written

$$(\Delta E)_{\text{one period}} = \int_{\text{Period}} \Delta P dt = 2\pi \frac{\Delta P}{\omega}. \tag{4.7}$$

Plugging this and Eq. (4.6) into Eq. (2.13), the amplitude of oscillation as a function of drive frequency is

$$x_0(\omega) = \sqrt{\frac{2Q\Delta P(\omega)}{m\omega\omega_0^2}}. \tag{4.8}$$

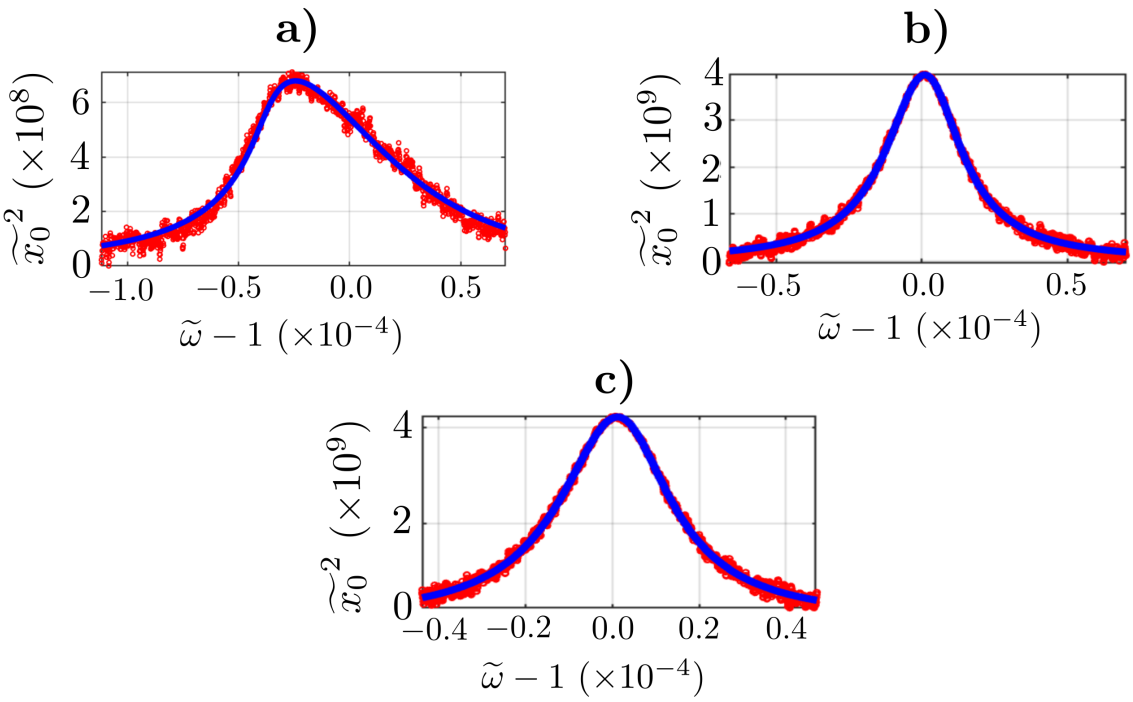

Figure 4.1: Example of fits of Eq. (1.43) (blue line) to experimental amplitude-frequency data (red circles) for states a) $He^4_\perp$, b) $He^3_\parallel$, and c) He_{nv} at 1.5 T. The experimental data has been smoothed with a rolling average filter.

4.3 Fit algorithm

Once the amplitude of oscillation has been extracted, Eq. (1.43) can be fitted to the $x_0^2(\omega)$ data, with f, α, and ζ free parameters. Resonant frequency is also allowed to vary by adding as another free parameter a perturbation ω_{dev} to ω_0. The fit parameters can then be tracked as functions of drive force, as given by Eq. (2.7), for different vortex states. For ease of comparison with previous and later work, the fit parameters are converted to their dimensionless forms in the plots that follow, defined in Section 1.3.3.

4.4 Fit results

The Duffing parameter as a function of drive force for states He_{nv}, $He^2_\parallel$, $He^3_\parallel$, $He^2_\perp$, $He^3_\perp$, and $He^4_\perp$ was estimated using the above fit algorithm. An example of fits of experimental data can been seen in Fig. 4.1. Drive force was modulated by changing

the magnetic field while holding drive power constant at 1 fW. Drive force was chosen as the independent variable over oscillation amplitude or beam velocity as drive force increases linearly with magnetic field, while velocity - and therefore amplitude - do not necessarily increase linearly with drive force as discussed in Section 3.2.

4.4.1 No-vortex and fully-trapped states

The Duffing parameter and drag coefficient as a function of drive force for states $He^1_{\parallel}$, $He^2_{\parallel}$, and He_{nv} at a drive power of 1 fW can be seen in Fig. 4.2. The Duffing parameter is positive, and the magnitude is small at low drive forces. At higher drive forces $\tilde{\alpha}$ increases in a close-to-linear fashion. Intrinsic nonlinearities, such as the geometrically-induced Duffing force described in Section 1.3.2, stiffen the resonator, yielding a positive Duffing parameter. The intrinsic Duffing force is proportional to the amplitude of oscillation, explaining the increase in $\tilde{\alpha}$ with increasing F_{Beam}.

The linear drag coefficient also increases with increasing drive force, but in a less linear manner. At low drive forces $\tilde{\zeta}$ is small and relatively constant. Once a critical point is reached, however, $\tilde{\zeta}$ increases super-linearly. The increase is consistent with an increase in drag due to turbulence nucleation by the resonator beam, as discussed in Section 3.2, and an increase in magnetomotive damping, as discussed in Section 3.1. The qualitative and quantitative behaviour of all three states is very similar, with the only significant divergence being $\tilde{\alpha}$ at high drive forces. The difference is well within the margin of uncertainty in the fits, however. This similarity is consistent with the similarity between no-vortex and fully-trapped states noted in Section 3.1 and Section 3.2.

4.4.2 Partially-trapped states

The Duffing parameter and linear drag coefficient as a function of drive force for states $He^2_{\perp}$, $He^3_{\perp}$, and $He^4_{\perp}$ at a drive power of 1 fW can be seen in Fig. 4.3. The value of $\tilde{\alpha}$ is negative and of greater magnitude than in the He_{nv} and $He_{\parallel}$ states. As force increases, a critical point is reached, after which $\tilde{\alpha}$ increases in magnitude nonlinearly. Greater oscillation appears to increase the influence of the partially-trapped vortex, manifesting as an increase in the magnitude of $\tilde{\alpha}$ with increasing drive force. The exact mechanism by which increased oscillation amplitude of the beam strengthens the negative nonlinear influence of the vortex is unknown. While a negative $\tilde{\alpha}$ is expected from the derivation in Section 4.1, the existence of a critical point is not. This behaviour is possibly due to competition between the intrinsic positive Duffing parameter and the vortex-induced negative parameter. At low drive forces, the vortex-induced nonlinearity may be balanced by the intrinsic nonlinearity, with the former beginning to dominate the latter only after the amplitude of oscillation is sufficiently

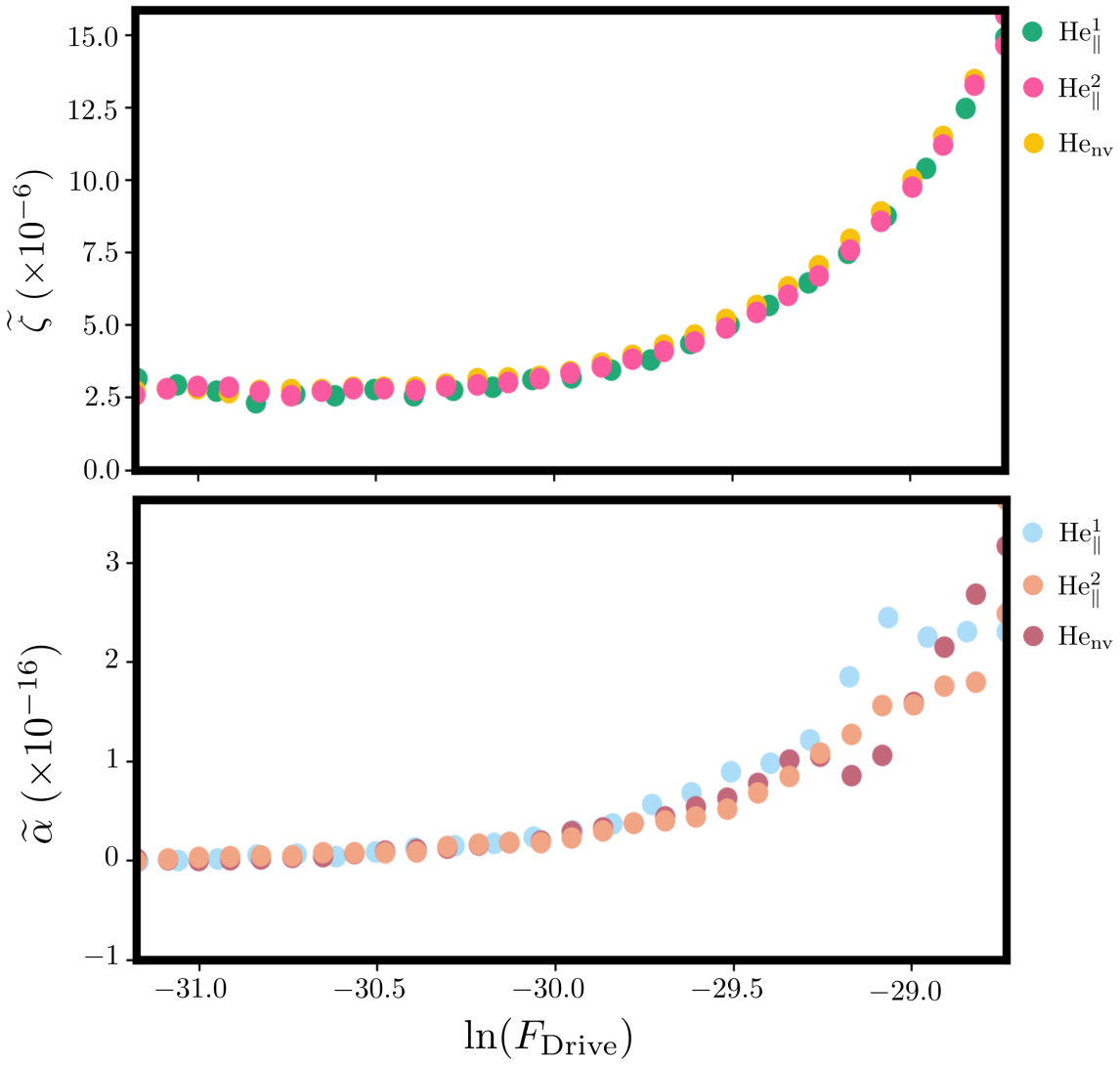

Figure 4.2: Dimensionless Duffing parameter $\tilde{\alpha}$ and linear damping $\tilde{\zeta}$ as a function of drive force F_{Drive} for states $\mathrm{He}_{\parallel}^{2}$, $\mathrm{He}_{\parallel}^{3}$, and $\mathrm{He}_{\mathrm{nv}}$ at a drive power of 1 fW. The increase in $\tilde{\zeta}$ is attributed to an increase in magnetomotive damping as higher drive forces are achieved by increasing magnetic field, as well as the onset of turbulence nucleation by the beam. The increase in $\tilde{\alpha}$ matches that expected of the geometrically-induced Duffing force discussed in Section 1.3.2.

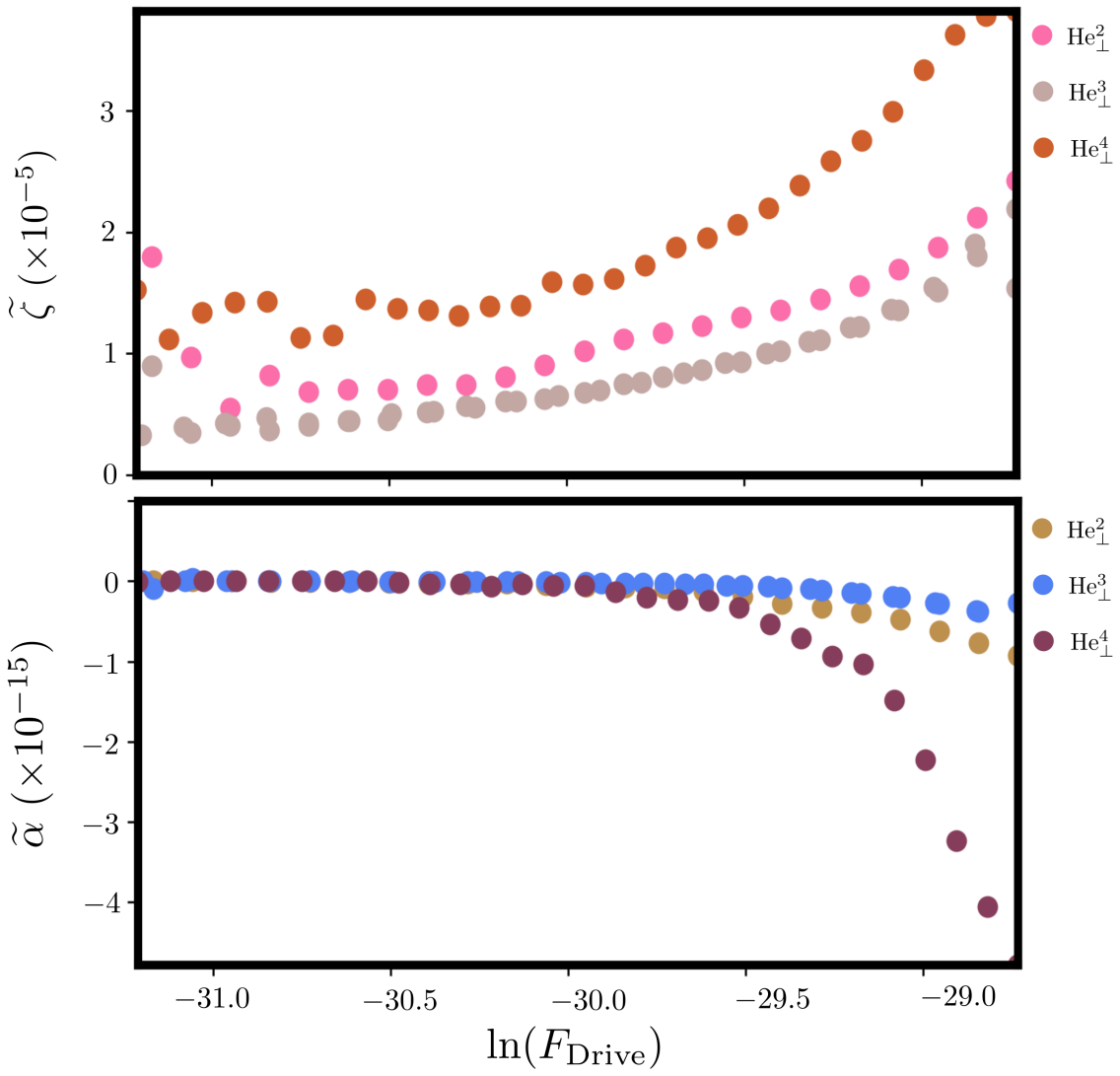

Figure 4.3: Dimensionless Duffing parameter $\tilde{\alpha}$ and linear damping $\tilde{\zeta}$ as a function of drive force F_{Drive} for states $\mathrm{He}_{\perp}^{2}$, $\mathrm{He}_{\perp}^{3}$, and $\mathrm{He}_{\perp}^{4}$ at a drive power of 1 fW. The increase in $\tilde{\zeta}$ is similar to that seen in no-vortex and fully-trapped states, though damping is of a higher magnitude at all drive forces - expected based on the increased losses in partially-trapped states described in Section 3.1. In contrast to no-vortex and fully-trapped states, $\tilde{\alpha}$ is negative, though magnitude still increases with increasing drive force. This behaviour is attributed to the unaligned vortex filament, via the mechanism discussed in Section 4.1.

large. Compared to fully-trapped and no-vortex states, $\tilde{\zeta}$ is greater in magnitude but displays the same qualitative behaviour as a function of drive force. This is consistent with the existence of additional dissipation in partially-trapped states, discussed in Section 3.1 and Section 3.2.

The qualitative behaviour of the three states is similar, with both $\tilde{\alpha}$ and $\tilde{\zeta}$ growing in magnitude with increasing drive force. The difference in quantitative behaviour between the three states does not correlate with resonant frequency or, therefore, the length of beam enveloped in circulation. The divergence could be related to the location of the pinning points on the resonator beam. A partially-trapped vortex that extends from the middle of the beam is likely to behave differently than a vortex extending from near to one of the ends, as any torque exerted by the vortex on the beam will have a greater effect far from the beam clamps. The Duffing and linear drag coefficients correlate with each other. States having a higher magnitude $\tilde{\alpha}$ also have a higher magnitude $\tilde{\zeta}$, suggesting that the mechanism by which a partially-trapped vortex induces a Duffing force and the mechanism by which it increases damping may be related.

Modelling the system as a driven-damped Duffing oscillator thus appears to support our other experimental observations. Linear drag increases with increasing drive force, with fully-trapped and no-vortex states possessing a nearly identical response and partially-trapped states exhibiting increased drag, in line with the findings presented in Section 3.1 and Section 3.2. The existence of a positive and increasing Duffing coefficient in fully-trapped and no-vortex states indicates that the largest drive forces achieved in this study are sufficient to introduce intrinsic nonlinearity to the system, and the overwhelmingly negative Duffing force seen in partially trapped states provides additional evidence that an unaligned filament attached to the beam can profoundly change the response of the resonator.

Chapter 5

Conclusions

The results of this work demonstrate several possible mechanisms by which the motion of single vortex filaments may be probed using a nanoelectromechanical resonator.

Analysis of the losses experienced by a doubly-clamped beam resonator and the relationship between peak beam velocity and drive force suggests a partially-trapped vortex introduces additional dissipation and drag beyond that present in a vortex-free resonator or a fully-trapped state. This is believed to be due to phonon emission by high-frequency Kelvin waves excited by the motion of the resonator beam. This suggests that dissipation in a trapped-vortex state could be used as a measure of Kelvin wave energy provided other loss mechanisms can be controlled for. The possible contribution of self-reconnections to these increased losses warrants further investigation. If a second beam resonator is placed near the primary device and the primary resonator is driven in a partially-trapped state at a velocity too low for the beam to nucleate turbulence, the observation of trapping events on the second resonator would provide strong evidence in favour of the self-reconnection model.

Phase modulation of the signal transmitted by the NEMS in partially-trapped states could provide further evidence for the motion of a single vortex filament influencing NEMS behaviour. The presence of frequency sidebands with uniform spacing across many partially-trapped states could be explained by a Helmholtz resonance coupling to the motion of the resonator. Since these sidebands are not seen in no-vortex and fully-trapped states, it is evidently the unaligned filament that facilitates the coupling, though the manner in which this could happen is currently unknown. Further experiments will modulate pressure in the sample cell, which is known to alter core radius and therefore Kelvin wave velocity[19]. If Kelvin waves are involved, a change in sideband spacing should be observable as pressure increases. Altering the length of the pipe leading to the sample cell will allow the existence of a Helmholtz resonance to be confirmed or refuted.

Modelling the NEMS-vortex system as a driven-damped Duffing oscillator

provides a compelling means of quantifying the changing behaviour of the NEMS due to both intrinsic and extrinsic nonlinear forces. Intrinsic geometric and mechanical nonlinearities tend to introduce a positive nonlinear restoring force that increases with increasing drive force, effectively hardening the resonator as the beam material resists stretching during high-amplitude oscillations. The presence of a partially trapped vortex introduces an overwhelming negative nonlinear restoring force, explained by the tension of the unaligned vortex filament. A means of mathematically quantifying the degree and direction of nonlinear behaviour in trapped-vortex states will permit easier comparison of different states. Applying this model to past and future data and tracking nonlinearity as a function of drive force and other independent variables could potentially reveal previously overlooked patterns and anomalies in the data that warrant further investigation.

The results of this work recommend the nanoelectromechanical vortex trapping scheme for further studies of Kelvin wave dynamics on individual vortices. The action of Kelvin waves in partially trapped states can be transduced by the resonator, manifesting as increased dissipation and, possibly, a negative nonlinear restoring force and modulation of the resonator's motion. This potentially provides a means of better experimental understanding of small-scale motion in individual quantum vortices, and therefore the as-yet poorly investigated Kelvin cascade.

Appendix A

Estimate of Intrinsic Duffing Parameter

To see how additional tension in the beam can lead to a Duffing-type nonlinearity, consider the Euler-Bernoulli equation for a thin oscillating beam of equilibrium length L_0[70]

$$\rho A \frac{\partial^2 X}{\partial t^2} = -EI \frac{\partial^4 X}{\partial z^4} + T \frac{\partial^2 X}{\partial z^2}, \tag{A.1}$$

where ρ is density, A is the cross-sectional area of the beam, E is Young's modulus, I is the moment of inertia, T is tension, X is displacement, t is time, and z is position along the length of the beam, with one clamp at $z = 0$ and the other at $z = L_0$. Let ΔL be the extension of the length of the beam due to stretching during oscillation. Stretching will induce an additional strain ΔT beyond the equilibrium tension T_0, so

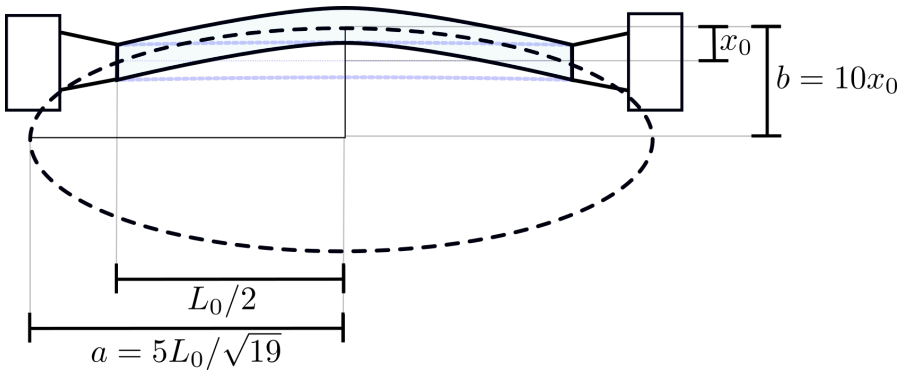

Figure A.1: Resonator beam modelled as a segment of an ellipse.

that $T = T_0 + \Delta T$. The additional strain is related to the length extension via

$$\Delta T = \frac{\Delta L E A}{L_0}. \tag{A.2}$$

The total length of the beam when stretched $L = L_0 + \Delta L$ is the line integral along the displaced beam which, via a first-order Taylor expansion, gives

$$\begin{aligned} L = L_0 + \Delta L &= \int_0^{L_0} \sqrt{1 + \left(\frac{\partial X}{\partial z}\right)^2} dz \\ &\approx \int_0^{L_0} \left(1 + \frac{1}{2}\left(\frac{\partial X}{\partial z}\right)^2\right) dz \\ &= L_0 + \frac{1}{2}\int_0^{L_0} \left(\frac{\partial X}{\partial z}\right)^2 dz. \end{aligned} \tag{A.3}$$

Eq. (A.1) then becomes

$$\rho A \frac{\partial^2 X}{\partial t^2} = -EI\frac{\partial^4 X}{\partial z^4} + \left(T_0 + \frac{EA}{2L_0}\int_0^{L_0} \left(\frac{\partial X}{\partial z}\right)^2 dz\right)\frac{\partial^2 X}{\partial z^2}. \tag{A.4}$$

This equation can be solved assuming the ΔT term is a perturbation and the solution to the linear component can be separated into temporal and spatial components $X = x(t)\phi(z)$[81]. Without loss of generality, let $\phi(z) = 1$ at the point of maximum displacement, so that $x(t)$ is the maximum displacement of any point on the beam. Multiplying Eq. (A.4) by $\phi(z)$ and integrating over z yields

$$\begin{aligned} 0 =& \rho A \frac{d^2 x}{dt^2}\int_0^{L_0} \phi^2 dz + EIx\int_0^{L_0} \phi\frac{d^4\phi}{dz^4} dz - T_0 x\int_0^{L_0} \phi\frac{d^2\phi}{dz^2} dz \\ &- \frac{EAx^3}{2L_0}\left(\int_0^{L_0}\left(\frac{d\phi}{dz}\right)^2 dz\right)\left(\int_0^{L_0}\phi\frac{d^2\phi}{dz^2}dz\right). \end{aligned} \tag{A.5}$$

Integrating by parts then gives

$$\begin{aligned} 0 =& \left[\rho A\int_0^{L_0}\phi^2 dz\right]\frac{d^2x}{dt^2} + \left[EI\int_0^{L_0}\left(\frac{d^2\phi}{dz^2}\right)^2 dz + T_0\int_0^{L_0}\left(\frac{d\phi}{dz}\right)^2 dz\right]x \\ &+ \left[\frac{EA}{2L_0}\left(\int_0^{L_0}\left(\frac{d\phi}{dz}\right)^2 dz\right)^2\right]x^3. \end{aligned} \tag{A.6}$$

where the cross-terms are zero since clamping requires $\phi(0) = \phi(L_0) = \phi'(0) = \phi'(L_0) = 0$. Stretching thus introduces a Duffing term, with a positive coefficient that increases with increasing bending of the beam.

The value of the expected intrinsic Duffing parameter of our beam can be estimated using this derivation. Assume that the amplitude of oscillation of the beam is $x_0 = 10^{-8}\,\mathrm{m}$, approximately the maximum observed experimentally. When the beam is at the point of maximum deflection, it can be modelled as a segment of an ellipse with minor axis $b = 10^{-7}$ and major axis

$$a = \sqrt{\frac{(L_0/2)^2}{1 - \left(\dfrac{b - x_0}{b}\right)^2}} = 8.03 \times 10^{-5}, \tag{A.7}$$

where L_0 is 70 µm. The segment of this ellipse corresponding to the deflected beam is illustrated in Fig. A.1. The position function $\phi(z)$ in Eq. (A.6), with $z = 0$ now fixed at the centre of the beam, is thus

$$\phi(z) = b\sqrt{1 - \frac{z^2}{a^2}} - (b - x_0), \quad -\frac{L_0}{2} \leq z \leq \frac{L_0}{2}. \tag{A.8}$$

The derivative is

$$\phi'(z) = -\frac{b}{a}\frac{z}{\sqrt{a^2 - z^2}}. \tag{A.9}$$

The intrinsic Duffing parameter suggested by Eq. (A.6), normalised to the effective mass of the resonator, is therefore

$$\alpha_{\text{intrinsic}} = \frac{\dfrac{EA}{2L_0}\left(\displaystyle\int_{-L_0/2}^{L_0/2}\left(\frac{b}{a}\right)^2\frac{z^2}{a^2 - z^2}dz\right)^2}{\rho A \displaystyle\int_{-L_0/2}^{L_0/2}\left(\frac{b}{a}\sqrt{a^2 - z^2} - (b - x_0)\right)^2 dz}. \tag{A.10}$$

Given that E is approximately 70 GPa; the height and width of the beam are 130 nm and 200 nm respectively, giving $A = 2.6 \times 10^{-14}\,\mathrm{m}^2$; and the combined density of the silicon nitride and aluminium is $\rho = 3062\,\mathrm{kg\,m^{-3}}$, $\alpha_{\text{intrinsic}}$ is approximately $2.6 \times 10^9\,\mathrm{m^{-2}\,s^{-2}}$.

Bibliography

[1] A. M. Guénault and T. Guenault, *Basic Superfluids* (CRC Press LLC, London, UNITED KINGDOM, 2002).

[2] K. R. Atkins, *Liquid Helium* (Cambridge University Press, Cambridge, UNITED KINGDOM, 1959).

[3] D. J. Griffiths and J. F. Allen, Proceedings of the Royal Society of London. Series A. Mathematical and Physical Sciences **277**, 214 (1964).

[4] U. Frisch and S. A. Orszag, Physics Today **43**, 24 (2008).

[5] C. Foias, P. Flajolet, O. Manley, R. Rosa, R. Temam, G.-C. Rota, B. Doran, M. Ismail, T. Y. Lam, and E. Wutwak, *Navier-Stokes Equations and Turbulence* (Cambridge University Press, Cambridge, UNITED KINGDOM, 2001).

[6] H. Yokoyama, H. Odawara, and A. Iida, International Journal of Aerospace Engineering **2016**, 1 (2016).

[7] R. H. Scanlan, Journal of Structural Engineering **123**, 232 (1997).

[8] L. Gao, S. Yang, A. Abraham, and J. Hong, Journal of Wind Engineering and Industrial Aerodynamics **199**, 104137 (2020).

[9] M. J. Pueschel, D. R. Hatch, D. R. Ernst, W. Guttenfelder, P. W. Terry, J. Citrin, and J. W. Connor, Plasma Physics and Controlled Fusion **61**, 034002 (2019).

[10] A. A. Schekochihin and S. C. Cowley, Physics of Plasmas **13**, 056501 (2006).

[11] P. S. Bernard, *Turbulent Fluid Flow* (John Wiley & Sons, Incorporated, Hoboken, UNITED STATES, 2019).

[12] W. J. Kwon, J. H. Kim, S. W. Seo, and Y. Shin, Physical Review Letters **117**, 245301 (2016).

[13] V. S. L'vov, S. V. Nazarenko, and O. Rudenko, Physical Review B **76**, 024520 (2007).

[14] C. F. Barenghi, Physica D: Nonlinear Phenomena Euler Equations: 250 Years On, **237**, 2195 (2008).

[15] M. Tsubota, Journal of Physics: Condensed Matter **21**, 164207 (2009).

[16] J. C. Wheatley, Reviews of Modern Physics **47**, 415 (1975).

[17] P. Kapitza, Nature **141**, 74 (1938).

[18] I. Ferrier-Barbut, M. Delehaye, S. Laurent, A. T. Grier, M. Pierce, B. S. Rem, F. Chevy, and C. Salomon, Science **345**, 1035 (2014).

[19] R. Donnelly, *Quantized Vortices in Helium II*, Cambridge Studies in Low Temperature Physics No. 3 (Cambridge University Press, Cambridge, UNITED KINGDOM, 1991).

[20] T. Simula, *Quantised Vortices: A Handbook of Topological Excitations* (Morgan & Claypool Publishers, San Rafael, UNITED STATES, 2019).

[21] A. Schmitt, *Introduction to Superfluidity – Field-Theoretical Approach and Applications*, Lecture Notes in Physics No. 888 (Springer International Publishing, Cham, SWITZERLAND, 2015).

[22] D. R. Allum, P. V. E. McClintock, A. Phillips, R. M. Bowley, and W. F. Vinen, Philosophical Transactions of the Royal Society of London. Series A, Mathematical and Physical Sciences **284**, 179 (1977).

[23] N. B. Brauer, S. Smolarek, E. Loginov, D. Mateo, A. Hernando, M. Pi, M. Barranco, W. J. Buma, and M. Drabbels, Physical Review Letters **111**, 153002 (2013).

[24] A. Del Maestro and B. Rosenow, Physical Review B **95**, 140507 (2017).

[25] O. Avenel and E. Varoquaux, Physical Review Letters **55**, 2704 (1985).

[26] D. I. Bradley, M. J. Fear, S. N. Fisher, A. M. Guénault, R. P. Haley, C. R. Lawson, G. R. Pickett, R. Schanen, V. Tsepelin, and L. A. Wheatland, Physical Review B **89**, 214503 (2014).

[27] R. P. Feynman, in *Progress in Low Temperature Physics*, Vol. 1, edited by C. J. Gorter (Elsevier, 1955) pp. 17–53.

[28] W. F. Vinen and D. Shoenberg, Proceedings of the Royal Society of London. Series A. Mathematical and Physical Sciences **260**, 218 (1961).

[29] L. Skrbek, Journal of Physics: Conference Series **318**, 012004 (2011).

[30] G. W. Rayfield and F. Reif, Physical Review **136**, A1194 (1964).

[31] R. Feynman, *Statistical Mechanics : A Set Of Lectures*, Advanced Book Classics (CRC Press, Boca Raton, UNITED STATES, 1998).

[32] M. L. Baehr, L. B. Opatowsky, and J. T. Tough, Physical Review Letters **51**, 2295 (1983).

[33] W. F. Vinen, Journal of Low Temperature Physics **145**, 7 (2006).

[34] D. I. Bradley, Physical Review Letters **84**, 1252 (2000).

[35] F. Hussain and K. Duraisamy, Physics of Fluids **23**, 021701 (2011).

[36] P. R. Schatzle, *An Experimental Study of Fusion of Vortex Rings*, Ph.D. thesis, California Institute of Technology (1987).

[37] A. T. A. M. de Waele and R. G. K. M. Aarts, Physical Review Letters **72**, 482 (1994).

[38] M. Kursa, K. Bajer, and T. Lipniacki, Physical Review B **83**, 014515 (2011).

[39] J. Koplik and H. Levine, Physical Review Letters **71**, 1375 (1993).

[40] S. Zuccher, M. Caliari, A. W. Baggaley, and C. F. Barenghi, Physics of Fluids **24**, 125108 (2012).

[41] R. Tebbs, A. J. Youd, and C. F. Barenghi, Journal of Low Temperature Physics **162**, 314 (2011).

[42] U. Giuriato and G. Krstulovic, Physical Review B **102**, 094508 (2020).

[43] M. S. Paoletti, M. E. Fisher, and D. P. Lathrop, Physica D: Nonlinear Phenomena At the Boundaries of Nonlinear Physics, Fluid Mechanics and Turbulence: Where Do We Stand? Special Issue in Celebration of the 60th Birthday of K.R. Sreenivasan, **239**, 1367 (2010).

[44] M. Leadbeater, T. Winiecki, D. C. Samuels, C. F. Barenghi, and C. S. Adams, Physical Review Letters **86**, 1410 (2001).

[45] B. V. Svistunov, Physical Review B **52**, 3647 (1995).

[46] W. Thomson, Proceedings of the Royal Society of Edinburgh **10**, 92 (1880).

[47] D. J. A. Roelvink and A. J. H. M. Reniers, *A Guide To Modeling Coastal Morphology* (World Scientific Publishing Company, Singapore, SINGAPORE, 2011).

[48] C. J. Nappo, *An Introduction to Atmospheric Gravity Waves* (Elsevier Science & Technology, San Diego, UNITED STATES, 2012).

[49] V. Bretin, P. Rosenbusch, F. Chevy, G. V. Shlyapnikov, and J. Dalibard, Physical Review Letters **90**, 100403 (2003).

[50] T. P. Simula, T. Mizushima, and K. Machida, Physical Review A **78**, 053604 (2008).

[51] E. Fonda, D. P. Meichle, N. T. Ouellette, S. Hormoz, and D. P. Lathrop, Proceedings of the National Academy of Sciences **111**, 4707 (2014).

[52] P. A. Davidson, *Turbulence: An Introduction for Scientists and Engineers* (Oxford University Press, Oxford, UNITED KINGDOM, 2004).

[53] W. F. Vinen and J. J. Niemela, Journal of Low Temperature Physics **128**, 167 (2002).

[54] A. N. Kolmogorov, V. Levin, J. C. R. Hunt, O. M. Phillips, and D. Williams, Proceedings of the Royal Society of London. Series A: Mathematical and Physical Sciences **434**, 9 (1991).

[55] W. F. Vinen, Physical Review B **61**, 1410 (2000).

[56] W. F. Vinen, Physical Review B **64**, 134520 (2001).

[57] M. Leadbeater, D. C. Samuels, C. F. Barenghi, and C. S. Adams, Physical Review A **67**, 015601 (2003).

[58] E. Kozik and B. Svistunov, Physical Review Letters **92**, 035301 (2004).

[59] V. V. Lebedev and V. S. L'vov, Journal of Low Temperature Physics **161**, 548 (2010).

[60] V. S. L'vov and S. Nazarenko, Low Temperature Physics **36**, 785 (2010).

[61] A. W. Baggaley and J. Laurie, Physical Review B **89**, 014504 (2014).

[62] E. V. Kozik and B. V. Svistunov, Journal of Low Temperature Physics **161**, 603 (2010).

[63] E. B. Sonin, Physical Review B **85**, 104516 (2012).

[64] V. V. Lebedev, V. S. L'vov, and S. V. Nazarenko, Journal of Low Temperature Physics **161**, 606 (2010).

[65] L. Boué, R. Dasgupta, J. Laurie, V. L'vov, S. Nazarenko, and I. Procaccia, Physical Review B **84**, 064516 (2011).

[66] N. P. Müller and G. Krstulovic, Physical Review B **102**, 134513 (2020).

[67] E. B. Sonin, JETP Letters **111**, 598 (2020).

[68] V. B. Eltsov and V. S. L'vov, JETP Letters **111**, 389 (2020).

[69] L. Kondaurova, V. L'vov, A. Pomyalov, and I. Procaccia, Physical Review B **90**, 094501 (2014).

[70] R. Lifshitz and M. C. Cross, in *Reviews of Nonlinear Dynamics and Complexity*, Vol. 1, edited by Heinz Georg Schuster (WILEY-VCH Verlag GmbH & Co. KGaA, Weinheim, GERMANY, 2008) pp. 1–49.

[71] J. Xu, B. You, and X. Li, in *2007 First International Conference on Integration and Commercialization of Micro and Nanosystems* (American Society of Mechanical Engineers Digital Collection, 2009) pp. 115–121.

[72] A. Guthrie, S. Kafanov, M. T. Noble, Y. A. Pashkin, G. R. Pickett, V. Tsepelin, A. A. Dorofeev, V. A. Krupenin, and D. E. Presnov, arXiv:2007.04482 [cond-mat, physics:physics] (2020), arXiv:2007.04482 [cond-mat, physics:physics] .

[73] M. Bao, *Analysis and Design Principles of MEMS Devices* (Elsevier B.V., Amsterdam, NETHERLANDS, 2005).

[74] D. I. Bradley, R. George, A. M. Guénault, R. P. Haley, S. Kafanov, M. T. Noble, Y. A. Pashkin, G. R. Pickett, M. Poole, J. R. Prance, M. Sarsby, R. Schanen, V. Tsepelin, T. Wilcox, and D. E. Zmeev, Scientific Reports **7**, 4876 (2017).

[75] R. J. Donnelly and C. F. Barenghi, Journal of Physical and Chemical Reference Data **27**, 1217 (1998).

[76] S. Ghaffari, E. J. Ng, C. H. Ahn, Y. Yang, S. Wang, V. A. Hong, and T. W. Kenny, Journal of Microelectromechanical Systems **24**, 276 (2015).

[77] D. I. Bradley, S. N. Fisher, A. Ganshin, A. M. Guénault, R. P. Haley, M. J. Jackson, G. R. Pickett, and V. Tsepelin, Journal of Low Temperature Physics **171**, 582 (2013).

[78] N. Hashimoto, R. Goto, H. Yano, K. Obara, O. Ishikawa, and T. Hata, Physical Review B **76**, 020504 (2007).

[79] Y. Nago, A. Nishijima, H. Kubo, T. Ogawa, K. Obara, H. Yano, O. Ishikawa, and T. Hata, Physical Review B **87**, 024511 (2013).

[80] C. Wang and J. C. S. Lai, Applied Acoustics **59**, 385 (2000).

[81] B. Yurke, D. S. Greywall, A. N. Pargellis, and P. A. Busch, Physical Review A **51**, 4211 (1995).